Electronic transport properties of hydrogenated amorphous silicon–germanium thin films

A DISSERTATION
SUBMITTED TO THE FACULTY OF THE GRADUATE SCHOOL
OF THE UNIVERSITY OF MINNESOTA
BY

Lis Stolik Valor

IN PARTIAL FULFILLMENT OF THE REQUIREMENTS
FOR THE DEGREE OF
DOCTOR OF PHILOSOPHY

James Kakalios, Adviser

January 2022

Acknowledgements

I'd like to thank my adviser James Kakalios for his constant support, encouragement, optimism, and guidance throughout grad school and this research. Professor, thank you for always believing in me.

During my time in the lab I had the pleasure to work alongside and discuss science with my fellow lab partners, Nathan Bosch, Brenda Knabuer, Raunaq Sharma, Ed Nguyen, and Blake Wendland. Ed was key in the measurement of the photoconductivity data here presented, which was a significant piece of information needed to further understand the a-SiGe:H sample's transport properties.

A special thanks to Ali Eslami Saray from the Mechanical Engineering Department, for depositing and determining the stoichiometry of the samples that later became my research project, and for useful discussions every time we bumped into each other in the lab.

Many of the faculty and staff at the University of Minnesota have contributed to this work. My gratitude to Prof Boris Shklovskii for his helpful suggestions and interest in this work. I'd like to thank Prof Renee Frontiera and Shahzad Alam in the Chemistry Department, for helping me determine the absorption data in a timely manner. Mike Rother consistently provided a helping hand in many of my ventures in the Physics student machine shop. The Characterization Facility staff were always helpful during my various characterization measurements.

My family was essential in my success during my PhD. For their insurmountable support, their love, understanding and for always providing objective advice when I needed it the most, thank you. To my parents for setting the best example I could ask for, and for always making me their number one priority. To my husband, for making me want to be my better self, for his encouragement and pep talks during hard times, and celebration and toasts during happy ones.

To my wonderful family

Abstract

Interest in amorphous semiconductors stems in part from their use in large–area thin–film applications, including photovoltaics, light–emitting diodes, thin film transistors, non–volatile memories and thermoelectrics. Furthermore, alloyed amorphous semiconductors have emerged as promising materials, as their optical bandgap can be easily engineered by controlling their chemical composition. Alloyed a-$Si_{1-x}Ge_x$:H thin film samples are fabricated in a dual–chamber plasma–enhanced chemical vapor deposition system, and a series of such films with Ge content ranging from (0 – 100)% are obtained. The Ge content is determined through X–ray photoelectron spectroscopy and qualitatively corroborated through measurements of their Raman spectra. Measurements of their dark conductivity, photoconductivity, and thermopower reveal a dual–channel conduction through the dangling bond states. Alloys with concentrations of Ge below 20% exhibit anomalous hopping conduction, while the dark conductivity of alloys with higher Ge concentrations are best fit by a combination of anomalous hopping at high temperatures and power–law temperature dependence for the low to mid–ranges, characteristic of multi–phonon hopping transport. The samples' photoconductivies show evidence of high defect state densities in the mid–gap. Corresponding measurements of the thermopower find that conduction is n–type for the purely a-Si:H and a-Ge:H samples but that the Seebeck coefficient exhibits a transition from negative to positive values as a function of Ge content and temperature. A conduction model involving the parallel contributions of the two distinct conduction mechanisms is shown to describe both the conductivity and the thermopower data to a high degree of accuracy. The clear experimental evidence of hopping conduction reported here provides important information concerning the nature of electronic conduction in amorphous semiconductors, and suggests that the concept of a mobility edge, accepted for over four decades, may not be necessary to account for charge transport in certain amorphous semiconductors.

Contents

List of Tables

List of Figures

Chapter 1

Introduction

Interest in amorphous semiconductors stems in part from their use in applications that do not require the high electronic mobility of single crystal materials, but rather call for semiconductors to cover large surface areas on a variety of substrate surfaces at low cost [1–3]. To list just a few examples, the replacement of cathode ray tube displays with light–weight, low–power flat panel liquid crystal displays was facilitated in part by advances in the fabrication of hydrogenated amorphous silicon (a-Si:H) based thin film transistors that modulate the optical properties of the large array of liquid crystal pixels [4]. Photovoltaic devices require large surface areas to maximize solar absorption, and while a-Si:H based solar cells have lower conversion efficiencies than crystal silicon (c-Si) based photovoltaics as well as stability issues, they can be easily deposited on a wide range of substrates (as there are no lattice matching constraints) over large areas at any desired thickness [5, 6]. Xerography [7] and medical X–ray imaging [8] also make use of the large area advantages of thin–film semiconductors, and amorphous semiconductors are promising candidate materials for high–energy particle detectors and satellite–based solar cells as their random atomic arrangements lead to them being less susceptible to damage following exposure to ionizing radiation than crystalline semiconductors [9–12].

Cost is a main advantage of using thin film amorphous Si in large scale production

of photovoltaic devices. The conventional method for the fabrication of single crystal silicon yields long cylinders with diameters of $\sim$ 12 inches that are sliced into thin wafers ($\sim$ 1 mm thick) and then processed to manufacture electronic devices. However, sunlight is absorbed within the first few microns, and the remaining thickness of the material is not efficiently utilized. Solar cells fabricated with amorphous semiconductors use only a fraction of the material needed for typical crystalline Si cells, and the cost of the silicon has historically been a significant contributor to cell cost. Not only that, but the deposition process of thin film amorphous silicon enables it to be deposited over large areas and thickness–tuned precisely in order to limit materials losses, unlike their crystalline counterpart, where the thickness is limited to hundreds of microns due to the physical limitations of cutting wafers from the silicon crystal ingot.

It is possible to extend even further the capabilities of a-Si:H, by introducing an additional element, such as germanium, into its network. Alloying a-Si:H with germanium enables the reduction of the electronic gap between the conduction and valence bands, while alloying a-Si:H with carbon results in a larger optical gap. Given that the element content x can be varied continuously in the alloying process, the bandgap can be similarly varied. This alteration of the optical absorption edge is employed in tandem solar cell structures, where a-Si:H is sandwiched between alloys of Ge and C, where the a-SiGe:H alloy is used to absorb lower energy photons and a-SiC:H to absorb higher energy light.

In this thesis, I will present detailed studies of the electronic and thermoelectric properties of a-$Si_{1-x}Ge_x$:H thin film samples as the Ge concentration x is continuously varied. This project is motivated not only by possible technological applications, but by an interest in understanding the fundamental transport mechanisms present in these materials. Recent studies have found that the standard model for electronic conduction in a-Si:H is not correct, and that charge transport proceeds via an anoma-

lous hopping mechanism, raising the question as to whether this holds for alloys of amorphous silicon.

In this chapter, I will begin with a brief introduction to the properties of thin film a-Si:H, including a discussion of the relevant electronic transport physics and a review of previous research done by other groups. Chapter 2 contains descriptions of the material's preparation, as well as a discussion of the structural and optical characterization, and measurement techniques employed in this work. The structural and optical results obtained will be described in chapter 3. The temperature dependence of the dark conductivity and thermopower, and the photoconductivity properties as a function of Ge content are presented in chapter 4. Discussion of these results, in the framework of recent investigations are presented in chapter 5. Finally, the conclusions and future outlook will be presented in chapter 6.

1.1 Electronic Transport in a-Si:H

Silicon and germanium are fourfold coordinated atoms, normally tetrahedrally bonded to four neighboring atoms. In its crystalline form this tetrahedral bonding results in the diamond crystal structure, that extends over a large range. In amorphous silicon or germanium this long–range order is not present. Tetrahedrally–bonded amorphous semiconductors such as a-Si:H and a-Ge:H exhibit disorder on many different length scales. Measurements of the radial distribution function from X–ray and neutron scattering in a-Si:H find that, compared to c-Si, the bond length and bond angle differ by only $<1\%$ and 10%, respectively, while there are significant variations ($> 35\%$) in the dihedral angle distributions [13]. Consequently, the correlation between the locations of Si atoms on length scales greater than the next–nearest neighbor ($\sim$1 nm) is essentially random in a-Si:H. In addition to this short–range disorder, there is considerable disorder on intermediate and long–range length scales ($\sim$

(10 – 100) nm), resulting from compositional modulations (microvoids and clusters of bonded hydrogen) and potential fluctuations from charged defects [5].

Amorphous Si or Ge fabricated without bonded hydrogen (such as by e–beam evaporation or sputtering) have a very high density ($\sim 10^{20}$ cm^{-3}) of dangling bond defects (Si or Ge atoms with only three covalent bonds and an unpaired sp^3 orbital). These materials cannot be impurity doped n–type or p–type as the high density of defects pins the Fermi energy in mid–gap. In addition, these materials are not photoconductive, as the dangling bond defects act as recombination centers, dramatically reducing the film's photosensitivity. These dangling bonds can be passivated by hydrogenating the amorphous silicon during film growth, either by sputtering in a hydrogen–rich atmosphere or by the plasma enhance chemical vapor deposition of silane (SiH_4) or germane (GeH_4). Hydrogen atoms bond to the dangling bonds, forming (in amorphous silicon) Si–H bonds and reducing the defect density by several orders of magnitude, to levels $\sim (10^{16} - 10^{17})$ cm^{-3}. The resulting hydrogenated amorphous silicon is more conductive, has a higher photosensitivity and can be doped by the addition of phosphorus (using PH_3 gas in the PECVD reactor) or boron (using B_2H_6). Doped a-Si:H, was first fabricated in 1969 by Chittick, Alexander and Sterling by deposition using a silane gas (SiH_4) precursor [5]. The resulting material showed a lower defect density and increased conductivity.

The existence of a continuous density of states (DOS) in a-Si:H is fundamentally different from the situation in crystalline semiconductors, where application of Bloch's theorem on an uniform crystal results in a gap between the highest energy occupied band and the lowest energy unoccupied band, where there are no available states for electrons to reside. In contrast, Bloch's theorem is not applicable in amorphous semiconductors due to the absence of a periodic crystal structure. In this case a generalized Tight Binding approach finds a continuous distribution of states between the highest energy occupied level and the lowest energy unoccupied state. The band

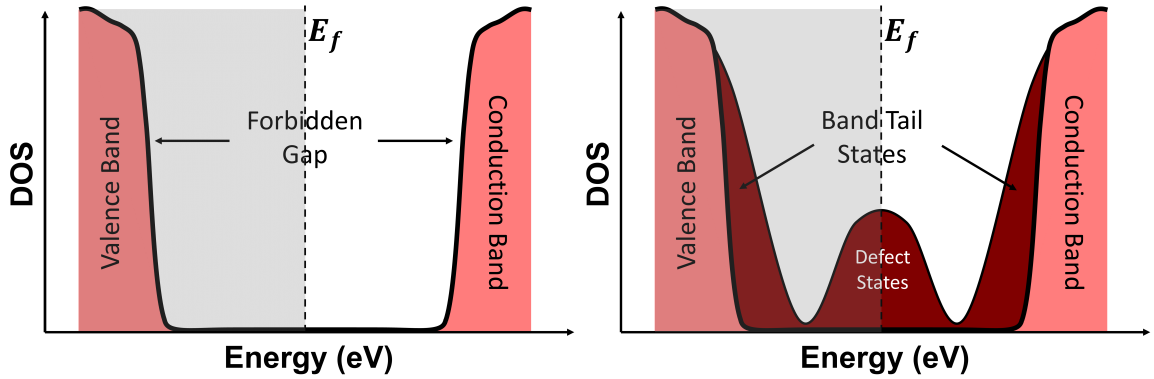

(a) (b)

Figure 1.1: Sketch of the density of states (DOS) for (a) crystalline silicon and (a) hydrogenated amorphous silicon (a-Si:H). The band edges in crystalline silicon are broadened in a-Si:H due to the disorder of the amorphous structure.

structures of a-Si:H and c-Si are sketched in Figure 1.1 to illustrate this difference.

Even though a-Si:H has no gap in the DOS, it has been proposed that there is a gap in the mobility of the charge carriers. This concept was introduced by Sir Neville Mott in 1967 [7] and can be described as follows. Conduction in a-Si:H occurs through charge carriers hopping between states of similar energy. Close to the Fermi energy, located within the defect dense mid–gap, the distance between nearby states is large, and very little current can flow. These localized states are primarily associated with dangling bond states, but also with strained Si–Si bonds [8]. As you move away from the Fermi level in either direction, the DOS increases exponentially, and the nearest neighbors' wavefunctions start to overlap, therefore allowing for hopping between states. These are bandtail states and arise from Si–Si bonds being stretched, compressed, twisted or otherwise altered from their lowest energy configuration. At a higher energy still, there is sufficient overlap between neighboring states that a charge carrier can move under an external bias for the length of the solid, and these states are termed "extended". The energy at which the nature of electronic states change from localized to extended states is termed the mobility edge.

In extended states above the mobility edge, the carriers' wavefunction overlap is sufficiently large that the free carriers behave as in a metal. In this case the sample's conductivity is limited only by the number of electrons excited into the high energy unoccupied band, or holes in the lower energy occupied band (analogs of the conduction and valence bands, respectively, in crystalline semiconductors). The Fermi energy is then taken to reside in the middle of this mobility gap.

The tails of the Fermi function f which extend past the mobility edge are exponentially dependent on the inverse of the temperature T:

$$f \sim \exp\left[-\left(\frac{\epsilon - \epsilon_F}{k_B T}\right)\right], \tag{1.1}$$

where ϵ_F is the Fermi energy and k_B is the Boltzmann constant.

The number of carriers at any energy is given by the product of the Fermi function and the DOS, which varies slowly with energy above the mobility edge. Therefore, we expect that the conductivity σ will follow an Arrhenius expression as a function of temperature. Assuming an n–type a-Si:H sample, the conductivity will be given by:

$$\sigma(T) = \sigma_o \exp\left[-\left(\frac{\epsilon_{CB} - \epsilon_F}{k_B T}\right),\right] \tag{1.2}$$

where ϵ_{CB} is the energy of the mobility edge separating the conduction band from the bandtail states and σ_o is a constant conductivity prefactor given by $N_c(\epsilon_{CB}) k_B T e \mu$, where $N_c(\epsilon_{CB})$ is the density of states at the conduction band edge, e is the electron charge, and μ is the free–carrier mobility in the extended states. Most researchers find that the a-Si:H conductivity is well described by Eq. (1.2), with activation energies, defined as $E_\sigma = \epsilon_{CB} - \epsilon_F$ between 0.8 and 1 eV [9–12], and prefactor $\sigma_o \sim 200$ $(\Omega\text{-cm})^{-1}$.

It is worth noting that Eq. (1.2) describes the conductivity behavior present in crystalline semiconductors as well, although its occurrence is due to a gap in the DOS,

rather than in the mobility.

At low enough temperatures, Eq. (1.2) yields a very small contribution to the conductivity, as there are too few free charge carriers in the extended states to carry significant current. In this case, charge transport results from electrons and holes trapped in localized defect states inside the bandgap that can tunnel from state to state, with a finite transition probability across the sample. For a charge in a given localized state, a state adjacent in space may in fact differ significantly in energy, reducing the hopping probability. Mott in 1968 proposed that charge transport in this case is a balance between tunneling to states that are similar in energy but far in space, and thermally excited hopping to nearby states. This effect is termed variable–range hopping (VRH), and for charge carriers hopping through nearby states close to the Fermi energy in a constant density of states [14], results in a conductivity temperature dependence given by

$$\sigma(T) = \sigma_o \exp\left[-\left(\frac{T_M}{T}\right)^{\frac{1}{4}}\right]. \tag{1.3}$$

T_M is the characteristic temperature in the Mott–type hopping described by

$$T_M = \frac{18}{k_B \alpha^3 \mathrm{DOS}(E_f)}, \tag{1.4}$$

where α is the localization length, $\mathrm{DOS}(E_f)$ is the density of states at the Fermi energy, and k_B is the Boltzmann constant.

At even lower temperatures another type of hopping conduction is seen in a variety of disordered semiconductors [15, 16], termed Efros–Shklovskii variable–range hopping (ES–VRH). This type of conduction, although similar to Mott's formulation, takes into consideration a Coulomb gap near the Fermi energy arising from Coulomb repulsion between occupied states, and can be expressed as [17]:

$$\sigma(T) = \sigma_o \exp\left[-\left(\frac{T_{ES}}{T}\right)^{\frac{1}{2}}\right]. \tag{1.5}$$

The characteristic temperature T_{ES} is

$$T_{ES} = \frac{2.8e^2}{4\pi k_B \varepsilon \alpha}, \tag{1.6}$$

where ε is the material's dielectric constant.

Recently, the conductivity of undoped a-Si:H [18], n–type doped a-Si:H [19] as well as composite films of a-Si:H containing nanocrystalline inclusions of either silicon or germanium (nc-Si or nc-Ge) [18] have been found to be described by an anomalous hopping expression:

$$\sigma(T) = \sigma_1 \exp\left[-\left(\frac{T_o}{T}\right)^{\kappa}\right], \tag{1.7}$$

where the exponent $\kappa \sim 0.75 \pm 0.05$. This behavior has also been found to describe the low temperature conductivity of ultra–thin disordered films of Ag, Bi, Pb and Pd [20]; of ultra–thin quench condensed Bi films [21]; of carbon–black polymer composites [22]; and of weakly coupled Au nanoparticles [23], ZnO quantum dot arrays [24] and two–dimensional electron glasses (2DEG) when a saturating magnetic field is applied parallel to the 2DEG [25, 26].

There is no accepted theoretical model for this conductivity temperature dependence. However, preliminary studies in a-Si:H [18] suggest that charge transport may be occurring through the exponential bandtails at a characteristic energy $\epsilon_t < \epsilon_{CB}$ (where ϵ_{CB} is the conduction band mobility edge) as proposed by Grünewald and Thomas [27] and Monroe [28].

This model can be understood as a transport mechanism in which carriers are thermally excited to the bandtail states, and variable–range hopping occurs through localized states. The main difference between this model and those describing the

Mott–VRH and ES–VRH formulations in that the hopping current flows through states near a transport energy ϵ_t, in general far from the Fermi energy level, while the Mott and Efros–Shklovskii VRH models describe hopping through states near the Fermi energy.

To precisely determine whether the temperature dependence of the dark conductivity can be described through an Arrhenius expression, Eq. (1.7) with $\kappa \neq 1$, or a power–law (discussed in Section 4.1), a reduced activation energy (W) analysis technique is used. In this procedure, developed by Zabrodskii and Shlimak [29], the logarithmic derivative of the conductivity, named the reduced activation energy, is computed:

$$W(T) = \frac{d \ln \sigma}{d \ln T}. \tag{1.8}$$

$W(T)$ is then plotted against temperature on a log–log plot, as shown in Figure 1.2. Each of the lines show calculations of the reduced activation energy for potential conductivity temperature dependencies given by Eq. (1.7) where the slope is equal to -1 (solid black), $-1/2$ (dashed red), $-1/4$ (short–dashed green), or 0 (dot–dashed blue). These slopes correspond to κ values for thermally activated conduction ($\kappa = 1$), ES–VRH ($\kappa = 1/2$), Mott VRH ($\kappa = 1/4$) and $\kappa = 0$ (where $\sigma \propto T^n$), respectively.

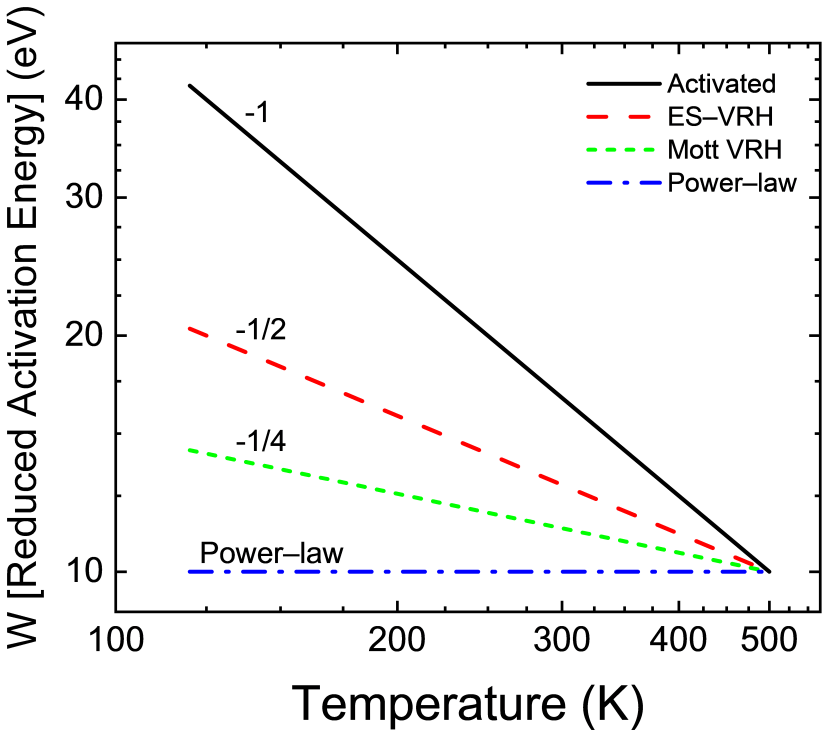

Figure 1.2: Log–log plot of the calculated reduced activation energy (W) against temperature for conductivity of the form of Eq. (1.7) for κ values corresponding to thermally activated ($\kappa = 1$) in solid black, Efros–Shklovskii variable range hopping (ES–VRH) ($\kappa = 1/2$) in dashed red, Mott variable range hopping (VRH) ($\kappa = 1/4$) in short–dashed green, and a power–law temperature dependence ($\kappa = 0$) in dot–dashed blue.

1.2 Photoconductivity of a-Si:H

Photoconductivity is an optoelectronic phenomenon where a semiconductor's electrical conductivity changes due to the absorption of electromagnetic radiation such as visible light, UV, or infrared (depending on the semiconductor's bandgap). Illumination with absorbing light can increase the density of electrons and holes in the conduction and valence bands, respectively, yielding an enhanced photoconductivity σ_{ph} that can be expressed as

$$\sigma_{ph} = e\mu G\tau_{rec}, \tag{1.9}$$

where G is the photogeneration rate, determined by the number of electron–hole pairs excited per unit volume per unit time, τ_{rec} is the recombination lifetime, e is the electron charge, and μ is the majority charge carrier's mobility. However, if these photo–excited charge carriers recombine before they are able to reach the electrodes, then the absorption of light does not result in an increase in the conductivity. Amorphous semiconductors typically have high mid–gap defect densities, making direct recombination of free electrons and holes less likely compared to indirect recombination via defect states, which have higher capture cross sections for free carriers.

The value of the photoconductivity is highly dependent on the light power density used. As the light power density is increased the quasi–Fermi level adjusts, moving through the electron trapping states towards the conduction band, and more and more trapping states are converted into recombination centers. This effect can be described through a power–law relationship between the steady state photoconductivity σ_{ph} and the light power density:

$$\sigma_{ph} \propto F^{\gamma}, \tag{1.10}$$

where F is the light power density or irradiance. This expression describes how

the number of free carriers increases with the light power intensity, while more trap centers are converted into recombination centers.

Different ranges of the γ exponent have been seen for different materials. For a-Si:H values of $0.6 < \gamma < 0.9$ have been reported [30].

Single crystal semiconductors with few trap states typically possess $\gamma = 0.5$, corresponding to bimolecular processes, or $\gamma = 1$, corresponding to monomolecular processes. In a bimolecular process the recombination is carried out by electrons and holes directly, and since $n = p$, their product is $np = n^2$, so the photoconductivity varies as $F^{1/2}$. In a monomolecular process, however, one sign of charge carrier becomes rapidly immobilized in a defect, and the photoconductivity depends only on the free–charge density. The monomolecular and bimolecular recombination processes are the two extreme cases observed in low–trap states simple crystalline semiconducting systems. An exponent γ lying between 0.5 and 1.0 requires a density of unoccupied recombination centers in the dark to be negligibly small. As well as trapping states within the bandgap to be exponentially distributed in energy. Then, experimental results of exponents γ lying between 0.5 and unity are strong evidence of a continuous distribution of states between the valence and conduction bands [31].

1.3 Seebeck Effect

The Seebeck or thermopower effect, is a method of measuring the entropy per unit charge carried by electrical currents in a material. When a temperature gradient is applied across a conductive sample, free charge carriers will diffuse from the hot end towards the cold end of the sample. In a material where the majority charge carriers are electrons, the electrons begin to accumulate at the cold end and a voltage difference is created across the sample with a negative potential at the cold end. The resulting electric field repels the electrons back towards the hot end, counteracting the

diffusion of more electrons, and the sample quickly develops a steady–state voltage. The Seebeck coefficient S is defined as the negative voltage induced per degree of temperature gradient in an open circuit,

$$S = -\frac{dV}{dT}. \tag{1.11}$$

Since the temperature gradient is responsible for the charge carriers' motion, it is possible to determine the sign of the majority charge carrier from the sign of the Seebeck coefficient S. A negative (positive) S indicates that electrons (holes) are the majority charge carriers in the sample.

This simple picture in which we treat the charge carriers as a gas is convenient for understanding the sign of the Seebeck coefficient, but it doesn't contain any information about the magnitude of S. Moreover, this treatment is not particularly accurate for the description of amorphous semiconductors, in which the carriers' mean free path is much shorter than in an ideal gas. In this case the magnitude of the Seebeck coefficient will depend on the carriers density of states, scattering rate, and mobility, as well as the material's bandgap and position of the Fermi energy level.

In a-Si:H, the drift mobility of electrons in the conduction band is roughly an order of magnitude larger than the mobility of holes in the valence band, resulting in a negative thermopower [32]. The thermopower can also depend on the slope of the DOS near the Fermi level. If the DOS is larger above the Fermi energy than below, electrons diffusion will be enhanced, and the electron–induced voltage will be larger than the hole–induced one, yielding a negative S. Materials with a single dominant charge carrier possess the largest thermopower, since the minority charge carrier produces an additive voltage of the opposite sign. When there is a very large dangling bond concentration and the motion of charge carriers occurs via hopping through the mid–gap defect states near the Fermi energy, the Seebeck coefficient is very sensitive to the slope of the density of states at the Fermi level, and can be either

positive or negative, depending on the mid–gap defect state energy densities and the position of the Fermi energy.

For a semiconductor with transport above the mobility edge, the thermopower is given by [33]:

$$S = \frac{k_B}{e}\left(\frac{\epsilon_{CB} - \epsilon_F}{k_B T} + A\right), \tag{1.12}$$

where A is the heat of transport and is given by $A = q + 5/2$. q is determined by the characteristic scattering mechanism present in the material. In a-Si:H, lattice scattering is expected to dominate, for which q takes the value of $-3/2$. Consequently, A is on the order of unity and is independent of temperature. The temperature dependence of the thermopower includes the term $(\epsilon_{CB} - \epsilon_F)$, which also appears in the conductivity (Eq. (1.2)). However, experimental measurements in a-Si:H and other amorphous semiconductors [34–36] have found that this energy, labeled E_S, when measured through the thermopower is smaller than that obtained in the conductivity (E_σ), sometimes by more than 0.2 eV.

An attractive application of the Seebeck effect is in thermoelectric devices. These are materials that generally have very large thermopowers and can drive a current from a temperature gradient or create a temperature gradient from an applied voltage (known as the Peltier effect). A large bandgap yields more energy transferred per charge carrier, which directly translates to a larger voltage. In general, semiconductors have the largest Seebeck coefficients, since the energy per charge carrier in metals is small, while insulators have very few charge carriers. Thermoelectrics have great technological promise, as they can use the waste heat from mechanical processes and convert it into usable electricity, increasing the efficiency of the system. They can also be used for refrigeration with no moving parts [37], as they can generate a temperature gradient given an applied voltage difference. The efficiency of a thermoelectric material can be expressed by the figure of merit zT, defined as

$$zT = \frac{S^2 \sigma T}{\kappa}, \tag{1.13}$$

where T is the temperature, σ is the electrical conductivity and κ is the thermal conductivity [38]. The largest figure of merit will be that of a material with the conductivity σ of a metal, the thermopower S of a semiconductor, and the thermal conductivity κ of an insulator.

Chapter 2

Materials Preparation and Characterization Techniques

This chapter focuses on the characterization techniques employed to study the samples in this thesis. In particular, we focus on the physics behind each technique, as well as on the technical procedure followed during our measurements.

First, the procedure to synthesize the samples is described, followed by the structural measurements used to understand their composition. Then, the methods used to determine the optical, electronic, and thermoelectric properties of these materials are discussed.

2.1 Material Synthesis

Hydrogenated amorphous silicon (a-Si:H) thin films are most commonly synthesized via plasma–enhanced chemical vapor deposition (PECVD) [5] and its many variants, including remote plasma deposition [39] expanding thermal plasma (ETP) [40] and very high frequency PECVD (VHF–PECVD) [41]. In these techniques a low–temperature plasma dissociates silane (SiH_4) into silicon and hydrogen radicals, which may then be deposited onto substrates in the plasma chamber.

During PECVD pure silane gas (SiH_4) flows between two parallel–plate electrodes

in a vacuum chamber, sketched in Figure 2.1. A radio–frequency power source of 4 W, at 13.56 MHz (electrode area of 62.2 cm^2, electrode separation of 2.4 cm), excites the silane molecule. There is an electronic level in SiH_4 approximately 12 eV above the ground state, for which the molecule is unstable against disassociation. A plasma is then formed, as one or more H atoms are removed from the silane molecules [42]. When both the plasma power and the silane partial pressure are low enough ($\sim$ 220 mTorr), very little recombination occurs, and a positive DC voltage builds up on the surfaces in the interior of the vacuum chamber due to the capture of the very mobile H^+ nuclei. This positive voltage attracts the heavier, negatively charged dissociated silane molecules, mainly in the form of SiH_3 radicals, and a thin film of a combination of Si, H, and dissociated SiH_4 grows on all exposed surfaces. The best quality films are grown with surface temperatures of $\sim$ (250 – 260) °C, which minimizes the mid–gap defect density as measured by electron spin resonance [43]. These temperatures increase the mobility of each deposited silane molecule, allowing it to "settle in" to its position relative to the Si and H atoms, and the system relaxes into a more energetically–favorable, yet still disordered configuration. Of particular importance is that at this temperature the hydrogen can diffuse enough to passivate defects in the network of Si atoms. At low growth temperatures there is insufficient surface diffusion of hydrogen and the defect density is comparatively increased. At too high a temperature, however, the diffusion of the hydrogen increases to the point that hydrogen is lost from the growing film, and there is a corresponding increase in defect density.

While not as extensively studied, hydrogenated amorphous germanium (a-Ge:H) is similar in many aspects to a-Si:H. Thin films of high quality a-Ge:H can be fabricated using PECVD in a similar configuration to that of a-Si:H, using germane gas (GeH_4) instead of silane. Using mixtures of SiH_4 and GeH_4, a-$Si_{1-x}Ge_x$:H samples with a gradual change in Ge content in varying ratios can be obtained.

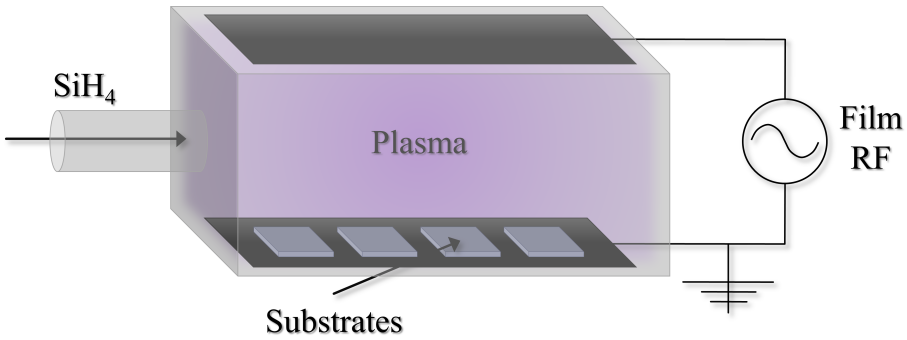

Figure 2.1: Sketch of a PECVD deposition chamber where a-SiGe:H thin films are grown.

2.2 Structural Characterization

2.2.1 X–Ray Photoelectron Spectroscopy (XPS)

The surface chemistry of the thin–film alloys is analyzed via X–ray photoelectron spectroscopy (XPS). The XPS spectrum is obtained by irradiating a solid surface with an X–ray beam. When an atom or molecule absorbs an X–ray photon, an electron can be ejected due to the photoelectric effect, and its kinetic energy (KE) depends upon the photon energy ($h\nu$) and the electron binding energy (BE). By measuring the kinetic energy of the emitted electrons, it is possible to ascertain which elements are near a material's surface (within the top (1 – 10) nm) by determining the binding energy of the electrons.

During XPS measurements a photoelectron spectrum is recorded by counting ejected electrons over a range of electron kinetic energies. Peaks appear in the spectrum from atoms emitting electrons of a particular characteristic energy, corresponding to the specific electron configuration within the atoms, e.g. 1s, 2s, 2p, etc. Each element produces a set of characteristic XPS peaks, and the number of detected electrons in each peak is directly related to the amount of a particular element within the sampling volume. The energies and intensities of the photoelectron peaks enable

quantitative identification of all surface elements (except hydrogen and helium, due to their lack of core electrons). Each peak area is proportional to the number of atoms present for each element. Therefore, the specimen's chemical composition is obtained by calculating the respective contribution of each peak area. To generate atomic percentage values, each raw XPS signal is corrected by dividing the intensity by a relative sensitivity factor (RSF), and normalized over all of the elements detected.

To demonstrate an XPS spectrum, a sample spectrum of a a-Si:H thin film is shown in Figure 2.2 for energies ranging from 75 eV to 175 eV. The spectrum shows peaks corresponding to Si_{2p} and Si_{2s}. Notice that both peaks have a "side peak" associated with them; these arise due to energy loss events such as non–elastic scattering of the photoelectric electrons by free electrons within the sample.

This spectrum, as well as all shown in this thesis, were taken using a PHI Versa Probe III XPS system with Al K_α X–ray radiation. There is a significant background below the peaks in the spectrum, which is caused by electrons that are inelastically scattered before leaving the sample surface. Such scattering reduces the kinetic energy of the detected electrons and reduces the peaks intensity. The background signals are removed from the spectrum before determining the elemental composition.

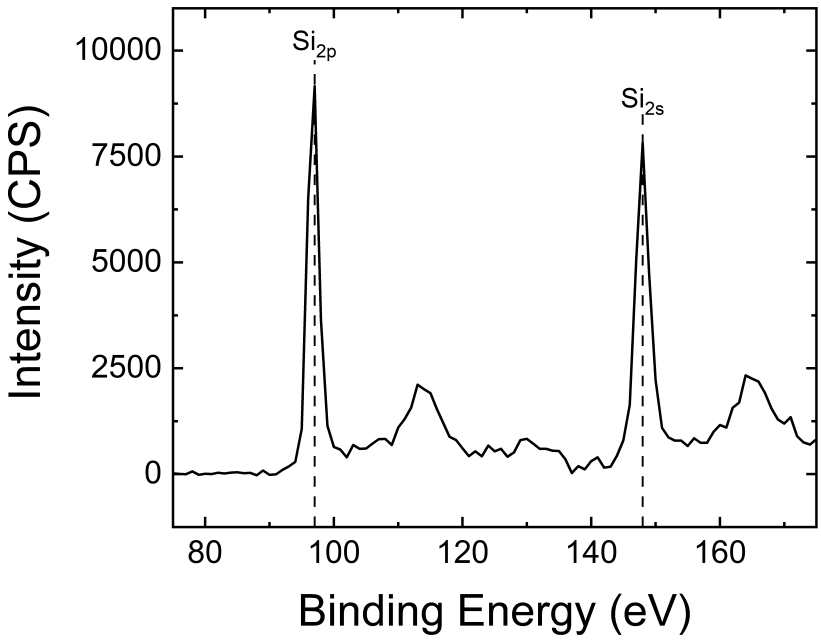

Figure 2.2: The Si_{2p} photoelectron and Si_{2s} peaks of a-Si:H.

2.2.2 Raman Spectroscopy

Raman spectroscopy analyzes the inelastic scattering of monochromatic light. A laser beam is incident on the sample, with the vast majority of the photons being scattered elastically via Rayleigh scattering, exciting and de–exciting with the same energy and, therefore, the same wavelength as the incident photons. A small fraction of the incident photons, however, interact with the bonds between atoms, exciting their vibrational modes. Changes in the wavelength of the scattered light appear as spectral peaks corresponding to different energies of excitation.

Raman scattering is contrasted with absorption of a photon in that absorption requires a permanent electric dipole moment, whereas Raman scattering has no such requirement. Rather, a dipole moment is induced by the incident electromagnetic field of the light, which allows observation of symmetric (Si–Si and Ge–Ge) vibrational

modes that are unavailable in absorption measurements. The spectra presented in this thesis will focus on stretching modes involving Si and Ge atoms.

The energy of a scattered photon can be either smaller or larger than the incident energy, corresponding to Stokes and anti–Stokes Raman scattering, respectively. The magnitude of the energy shift is sensitive to the atomic masses in the bonds as well as the strain and disorder in the lattice structure. Consequently, the Raman spectra can be used to determine the relative concentrations of different atoms and different phases in a sample. In this work, Raman spectroscopy will be used primarily to qualitatively verify the relative concentrations of Si and Ge resulting from the XPS analysis. We will also pay attention to the type of modes shown in the spectra, i.e. coming from Si–Si, Ge–Ge, or Si–Ge modes.

The energy shifts in Raman scattering are usually reported in units of wavenumber (cm^{-1}), mostly for historical reasons. In this thesis, we will only focus on the Stokes Raman scattering, in which the photons lose energy in order to excite a vibrational mode in the solid. In single crystals, the Raman spectrum consists of a single, very sharp peak at a single energy. For crystalline Si, the transverse optical (TO) mode peak is observed at $\sim$ 520 cm^{-1}, and for crystalline Ge, a corresponding TO mode peak is found at $\sim$ 300 cm^{-1}. In crystals, a single peak is observed because photons have very little momentum (k) to give to the crystal structure in comparison to a phonon. Momentum is conserved during Raman scattering and due to the dispersion relations and band structures in c-Si and c-Ge, there is only one single phonon mode that can be activated while maintaining momentum conservation, that is, the $k = 0$ point in the TO mode.

In amorphous silicon (or amorphous germanium), however, the lack of long–range order relaxes the requirement of momentum conservation. Any phonon that is activated can effectively "borrow" momentum from nearby defects and strained bonds, a feature that isn't available in single–crystals. This is reflected in a band of allowable

phonon energies, with each band appearing as a broadened Gaussian peak. A second consequence of the lack of long–range order is that, in addition to the TO mode, the other, non–k–conserving phonon modes can be activated during Raman scattering: transverse acoustic (TA), longitudinal optical (LO), or longitudinal acoustic (LA). As a result, the total Raman signal from the Si–Si (Ge–Ge) bonds in amorphous silicon (germanium) is composed of multiple Gaussian peaks, one from each population of phonon modes.

A sample Raman spectrum for a hydrogenated amorphous silicon thin film is shown in Figure 2.3. The total measured spectrum is decomposed into four separate peaks, each corresponding to a different phonon mode. The peaks for the TO, LO, LA, and TA modes all overlap somewhat, centered at 480 cm^{-1}, 410 cm^{-1}, 320 cm^{-1}, and 175 cm^{-1}, respectively. This results in many different possible fits accurately describing the data, where the widths, positions and heights of each peak vary considerably. As a consequence, the Raman spectra presented in thesis will only serve as qualitative data to support the samples stoichiometry resulting from more precise XPS measurements.

The amorphous germanium Raman spectrum is reminiscent of the amorphous silicon spectrum, with the TO mode at 278 cm^{-1}, the LO mode at 233 cm^{-1} and the LA mode at 175 cm^{-1}. When measuring a-SiGe:H samples, heterogeneous Si–Ge streching vibrational modes are also visible around 365 cm^{-1}.

The Raman data presented in this thesis were collected using a Witec Alpha 300R confocal Raman microscope, filtered to remove the Rayleigh signal at low energies. As a consequence, only the higher–energy tail of the TA peak is visible in the spectra presented here, and analysis of this peak is ignored. The microscope uses an argon–ion laser at 514.5 nm focused to a spot size of ~ 0.3 μm in diameter, a UHTS 300 spectrometer, and a DV401 CCD detector. The laser was carefully maintained at a low power level in order to minimize local heating of the sample, which can cause the peaks' locations to shift to lower wavenumbers by a few cm^{-1}.

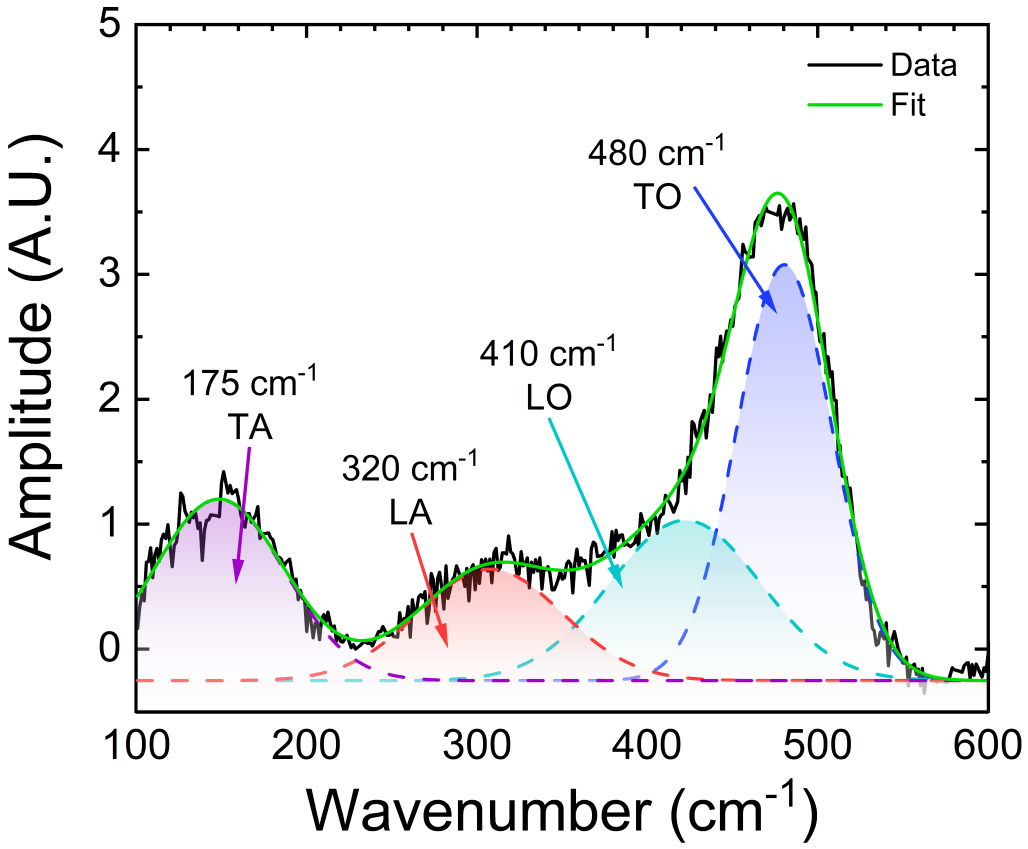

Figure 2.3: Raman spectrum of a pure a-Si:H thin film (black). The total measured spectrum can be decomposed into four separate Gaussian peaks, centered at 480 cm^{-1} (blue), 410 cm^{-1} (cyan), 320 cm^{-1} (red), and 175 cm^{-1} (purple), shown as dotted lines. The sum of these four peaks is shown by the solid green line.

2.2.3 Profilometry

The thickness and profile of the sample is determined by profilometry, in which a probe is dragged very lightly across the surface of the sample and the vertical movement of the probe is measured. The sample substrates under study were partially masked before deposition, in order to create a sharp edge in the film. Then, when scanning with the profilometer, passing from the bare substrate to the sample surface, the height of this edge, and therefore the film's thickness, can be determined. These measurements were carried out by a KLA–Tencor high definition Surface Profiler.

2.3 Optical Transmission

The optical transmission of a thin–film material can be obtained through an Ultraviolet–visible spectrophotometer (UV–Vis). This instrument measures the power density of light after passing through a sample (I), and compares it to that of the incident light (I_o). Assuming negligible light scattering, the ratio I/I_o is called the transmittance (T), and is usually expressed as a percentage. It is important to note however that the films' substrates also present spectral absorption. Then, the transmittance is given by

$$T = \frac{I_{\text{sample}}}{I_{\text{substrate}}}, \tag{2.1}$$

where I_{sample} is the data obtained when an amorphous film is measured, and $I_{\text{substrate}}$ is the data obtained when measuring a blank substrate.

Transmission measurements are used to obtain the optical absorption coefficient values of the amorphous films following the the Ritter–Weiser formula [44]:

$$\alpha d = \ln\left(0.5\left\{(1-R_2)\left(1+\frac{A}{T}\right)+\left[(1-R_2)^2\left(1+\frac{A}{T}\right)^2+4R_2\right]^{\frac{1}{2}}\right\}\right), \tag{2.2}$$

where $A = 1 - R - T$ (with R as the reflectivity of the front surface of the thin film and T as the transmittance), d is the sample thickness, and R_2 is the reflectivity of the back interface of the film. To determine R and R_2 the index of refraction of the sample and quartz substrate are used. Quartz has an index of refraction $n = 1.55$ [45]. Bhan et.al. [46] looked at the optical properties of six samples in a series of a-$Si_{1-x}Ge_x$ films prepared by reactive ion beam sputtering. Using a linear interpolation for each samples' reported n values, the index of refraction corresponding to each of our samples was determined.

A typical absorption spectrum for amorphous thin films is shown in Figure 2.4. Region A described as band–to–band absorption, corresponds to transitions between the extended states. The photons absorbed in this region are at an energy that is higher than that of the bandgap. Transitions concurring in region B involve at least one localized bandtail state, and is termed the bandtail absorption region. Here the absorption coefficient is the product of a slowly varying density of states and the bandtail states which vary exponentially with energy. The slope of alpha with $h\nu$ in this region is referred to as the Urbach slope ($\alpha \sim \exp[-h\nu/E_U]$) and provides a measure of the variation of the exponential bandtail states with energy. Bandtail absorption provides a measure of the disorder, such as strained bonds, in the film. Defect induced absorption is present into region C, and the magnitude of absorption in this region reflects the density of mid–gap defects. This region is not measured using transmission spectroscopy in low conductive films such as the undoped a-SiGe:H thin films studied here.

In the weak absorption regime the spectral reflectance of thin films gives rise to

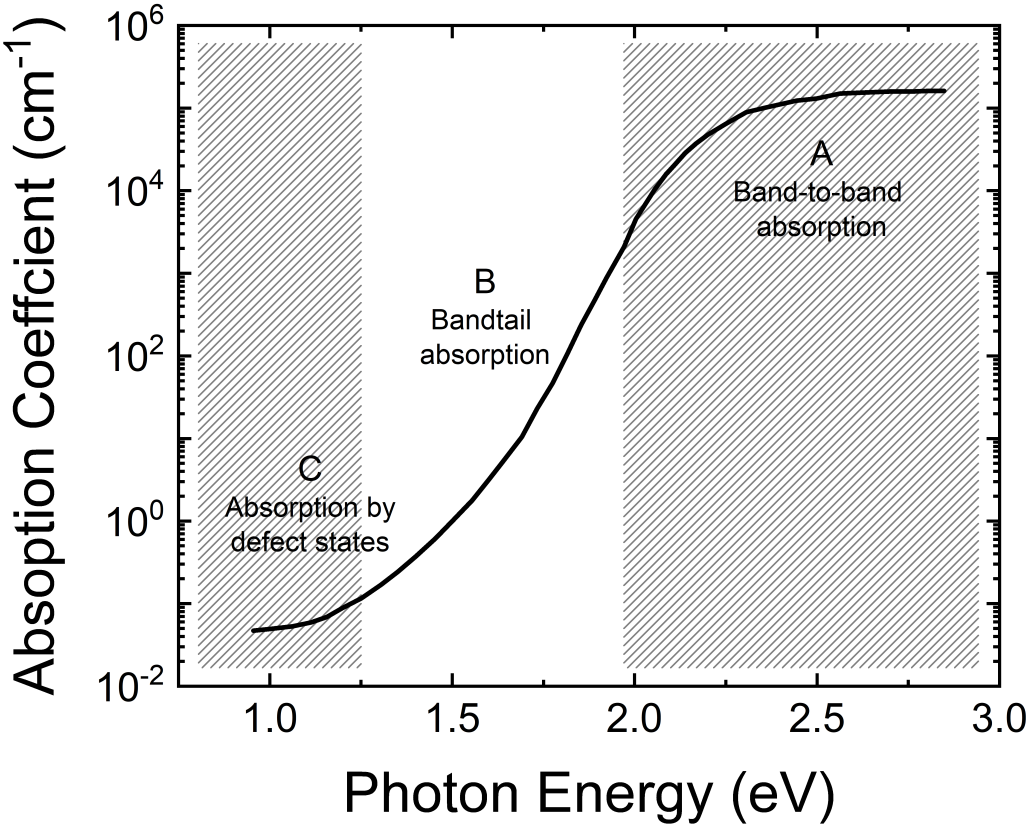

Figure 2.4: Typical absorption spectrum of an amorphous semiconductor. Region A corresponds to band–to–band absorption, region B to bandtail absorption, while region C is defect induced, and it is typically not seen in low conductive samples.

interference fringes. For the purpose of measuring α, this section of the spectra will be ignored.

Once the optical absorption spectra is obtained, we can construct a Tauc plot [47], from which we can extract information about the film's optical bandgap. These samples are well described by the expression

$$(\alpha h\nu)^{\frac{1}{2}} = B(h\nu - E_{opt}). \tag{2.3}$$

The slope B reflects the degree of order (i.e., wave function overlap between initial and final states) in the film, and the abscissa intercept provides a determination of the optical gap E_{opt}. This equation follows from the lack of wave vector conservation in an amorphous semiconductor and the optical gap defined by this relationship is typically referred to as the Tauc gap. A typical Tauc plot shows a linear region corresponding to the bandtail absorption region. By extrapolating this linear region to the abscissa, we can determine the energy of the optical bandgap E_{opt} of the amorphous material.

2.4 Electronic Characterization

2.4.1 Electrical Dark Conductivity

The simplest and most common transport measurement is the conductivity as a function of temperature. On the surface of the sample, two aluminum electrodes are evaporated in a coplanar configuration. The electrodes are up to $L = 1$ cm long, 500 nm thick, and the separation w between the two electrodes is 4 mm. Electrical contact is made with the electrodes by securing the end of a thin, bare Cu wire to each electrode with silver paint. Ideally, the silver paint acts only as a binding agent and current flows directly from the electrode to the wire. Poor electrical contact often leads to non–Ohmic transport; therefore all samples were tested for linear current–

voltage curves before any other measurements were made. At a given temperature, the current I is measured at a constant voltage V, and the conductivity is given as:

$$\sigma = \frac{I}{V}\,\frac{w}{Ld} \tag{2.4}$$

where d is the thickness of the film.

Dark conductivity measurements presented in this thesis were performed under vacuum in a LakeShore Janis closed–cycle He cryostat, sketched in Figure 2.5. The sample stage consists of a partially gold–plated copper block with an embedded 50 W cartridge heater. The sample stage is separated from the cryostat's cold head by a sapphire crystal, which has a low thermal conductivity to allow the sample stage to reach temperatures up to 500 K. At very low temperatures, however, the thermal conductivity of the sapphire is large enough to cool the sample stage down to 10 K. The temperature of the sample is monitored by a Si diode mounted next to the sample on the sample stage (T_{Sample}). A second sensor is placed near the heater to provide an input for the temperature controller ($T_{Control}$).

Conductivity measurements reported in this thesis were all performed in a two–probe configuration. A DC voltage of 100 V was applied across the sample and the current was measured by a Keithley 6517A femto–ammeter. Because the samples presented here are all undoped and very resistive, with resistances between 1 GΩ and 100 TΩ any contact resistances that may be present at the interfaces between the sample and electrodes are orders of magnitude smaller than the film's resistance, and negligible in our final current measurements.

2.4.2 Photoconductivity

Photoconductivity measurements were performed in a system similar to the closed–cycle system described in Section 2.4.1, although without the low temperature ca-

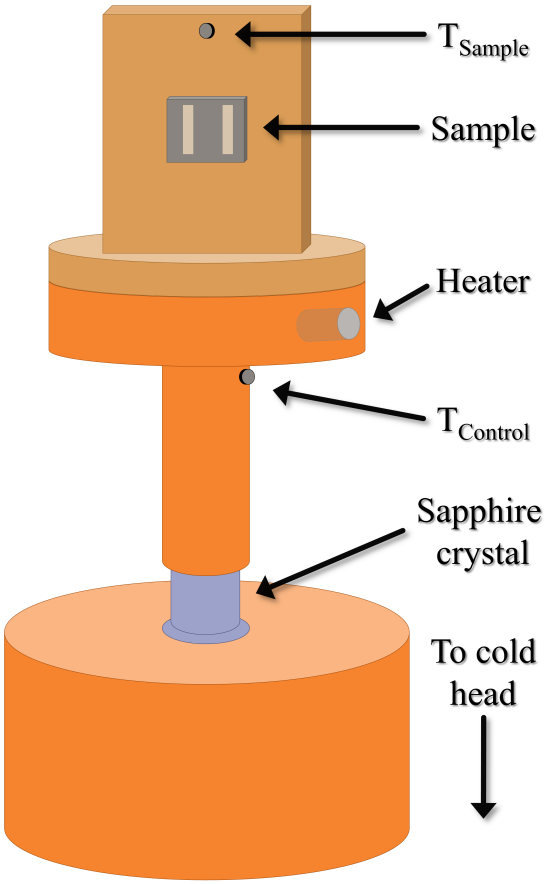

Figure 2.5: Cartoon of the sample stage in the closed–cycle He cryostat used for conductivity measurements presented in this thesis. The sample is attached to the stage using thermal grease, and electrical connections are made to the electrodes on the sample surface. The temperature sensor labeled "$T_{Control}$" is used by the temperature controller along with the heater to control the temperature of the stage. The sensor labeled "T_{Sample}" gives the temperatures reported in the data in this thesis. The sample can reach temperatures up to 500 K and is thermally separated from the cold head, which is always below 70 K, by a low thermal conductive sapphire crystal.

pabilities. The measurement system consists of a copper block with an embedded cartridge heater, upon which the sample is affixed with Ag paint to provide thermal coupling to the Cu block. A thermocouple is attached to a piece of glass mounted on the copper block next to the sample, so that the measured temperature is as close as possible to the real sample temperature and it is used as both the input for the temperature controller and the sample temperature. The entire system resides in a vacuum chamber with a window that filters infrared frequencies, to minimize sample heating while the light source is on. Measurements are made at pressures below 5 mTorr, and temperatures between room temperature and 480 K.

Samples undergo metastable conductivity changes upon exposure to light and ambient conditions. In order to return a sample to its pre–light–soaked state (state A) a two hour anneal process is administered at 480 K. Once in state A, the sample is cooled down to 305 K, and the dark conductivity is measured for a few minutes or until it is stable, while the temperature is kept constant. Subsequently, the film is illuminated with white light and the photoconductivity is measured. For this, a tungsten–halogen (W–Ha) lamp with power density $\sim$ 75 mW/cm^2 was utilized, as well as various neutral density filters used to vary the incident light power density. The measurement process begins with illumination using the lowest possible light irradiance. After 2 min of light exposure, illumination is stopped and the dark conductivity is again measured. This process is repeated for other light irradiances, always going from dimmer to brightest illumination.

The effective steady state photoconductivity can be defined as the difference between the measured photoconductivity σ_m and the dark, state A conductivity σ_A,

$$\sigma_{ph} = \sigma_m - \sigma_A. \tag{2.5}$$

It is expected for the photoconductivity σ_{ph} to obey a power–law relationship with the light intensity as in Eq. (1.10), with exponent γ between 0.5 and 1.

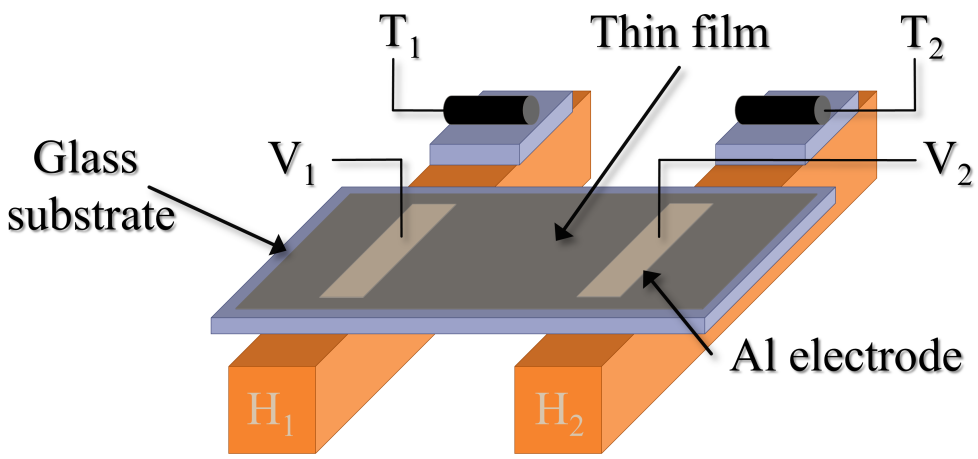

Figure 2.6: Sketch of the sample holder for thermopower measurements. The sample is placed so the electrodes are parallel to and atop two copper blocks, which each have an embedded heater (H_1 and H_2). The temperatures at each block are independently controlled using platinum resistors T_1 and T_2 as input sensors; these platinum resistors are mounted on glass slides so that their temperatures are comparable to the sample temperatures.

2.4.3 Thermopower

The thermopower measurements presented in this thesis were performed in a custom–made system. Inside a vacuum chamber capable of reaching $\sim$ 30 mTorr, the sample is placed across two separate copper blocks (H_1 and H_2 in Figure 2.6) such that the electrodes are directly above and resting on the copper blocks. Both the copper blocks and the electrodes on each sample presented here are separated by 4 mm. Inside of each copper block, a 50 W cartridge heater is embedded.

The temperature of each block is controlled independently by a dual–channel temperature controller, using platinum resistors (T_1 and T_2) attached to glass slides on each copper block as input sensors. The temperatures of the blocks T_1 and T_2 are set so that the average is $T_{avg} = \frac{T_1+T_2}{2}$ and the temperature gradient is $\Delta T = T_1 - T_2$. The temperature equilibration times are sufficiently long (2 min) to ensure an uniform temperature between the blocks and the sample surface.

The temperature gradient set across the sample electrodes induces a thermoelectric voltage ($V_1 - V_2$) in Figure 2.6) across the sample. For each average temperature, thermal gradients ΔT varying from $\pm$8 K with 1 K intervals are generated, and the respective induced voltages are recorded, eliminating contributions of any small temperature–dependent voltage offset to the signal [48]. Temperature stability is maintained within $\pm$0.05 K of the target temperature for at least 120 seconds before collecting the data. The entire measurement system is capable of measuring the electrical properties of high impedance thin films down to $\sigma \sim 10^{-10}$ (Ω-cm)$^{-1}$ while residing in a vacuum chamber [48]. The measured Seebeck coefficient is then derived from the slope of the resulting linear plot of induced voltage against ΔT, and the process is repeated at a new average temperature, from 320 K to 480 K.

Chapter 3

Structural and Optical Results of a-$Si_{1-x}Ge_x$:H thin films

This chapter discusses the effects of varying the Si/Ge ratio in an amorphous composite thin film series on the material's structural and optical properties.

3.1 X–Ray Photoelectron Spectroscopy (XPS)

The concentration of silicon and germanium varies in each film as the different relative silane and germane ratios were adjusted in the PECVD reactor chamber. The precise stoichiometry of the films is determined via X–ray photoelectron spectroscopy (XPS). By irradiating the sample with an X–ray beam we can obtain the characteristic electron population spectra of each element by counting ejected electrons over a range of electron kinetic energies.

The resulting XPS spectra for the a-$Si_{1-x}Ge_x$:H film series under study is presented in Figure 3.1. By calculating the respective contribution of each peak area in a particular sample, we were able to determine each samples' chemical composition. As a result, the samples are a-$Si_{1-x}Ge_x$:H films with variable Ge content with values: {0, 17, 48, 73, 93, 100}%. These differ from the expected Ge content, based on the GeH_4/SiH_4 ratios, set to be {0, 10, 25, 50, 75, 100}%.

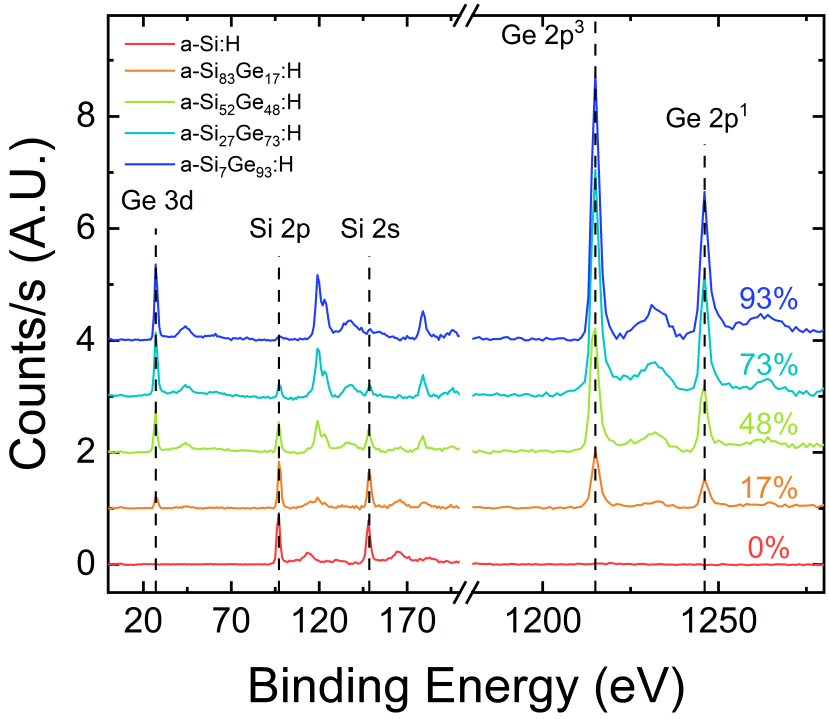

Figure 3.1: X–ray photoelectron spectra of a a-$Si_{1-x}Ge_x$:H film series. These measurements were used to determine the stoichiometry.

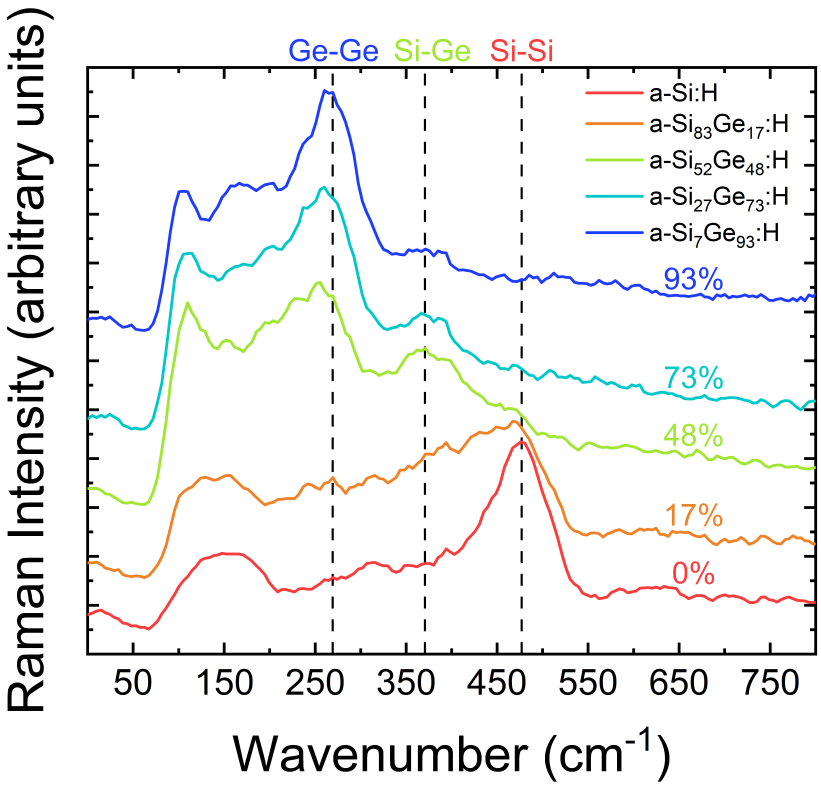

Figure 3.2: Raman spectra of a a-$Si_{1-x}Ge_x$:H film series. These measurements were used to confirm the relative Si/Ge content ratio as well as to detect if there is any crystallinity present in the samples.

3.2 Raman Spectroscopy

The qualitative relative Si and Ge content is confirmed through Raman spectroscopy, where the LO and TO modes of silicon and germanium are detected. The Raman spectra for the a-$Si_{1-x}Ge_x$:H film series are presented in Figure 3.2.

The spectra clearly shows peaks corresponding to the LA, LO, and TO modes of Si at 316, 395, and 476 cm^{-1}, respectively; as well as the LA, LO, and TO for Ge at 198, 233, and 269 cm^{-1}, respectively. There is an appreciable reduction of the Si–Si TO mode (at $\sim$ 476 cm^{-1}) and an increase of the Ge–Ge TO mode (at $\sim$ 269 cm^{-1})

as the Ge concentration determined by XPS increases. Under further inspection, the peak corresponding to the Si–Ge mode (at $\sim$ 371 cm^{-1}) appears in samples that are near the 50/50 SiGe ratio content.

No sharp Raman peaks were detected, either for Si or Ge, indicating that we are in the presence of fully amorphous samples.

3.3 Profilometry

Profilometry measurements carried out for the a-$Si_{1-x}Ge_x$:H thin film series gave thicknesses of $\sim$ 2 μm for most samples, except for the pure a-Si:H and a-Ge:H films. All samples' thicknesses are detailed in Table 3.1.

Sample	Thickness (μm)
a-Si:H	0.85
a-$Si_{83}Ge_{17}$:H	1.40
a-$Si_{52}Ge_{48}$:H	1.80
a-$Si_{27}Ge_{73}$:H	2.04
a-Si_7Ge_{93}:H	2.17
a-Ge:H	0.315

Table 3.1: Thicknesses in μm of the a-$Si_{1-x}Ge_x$:H sample series.

3.4 Optical Absorption and Bandgap

In this section we present the results of the optical absorption measurements performed on the a-$Si_{1-x}Ge_x$:H thin film series, using a standard UV–Vis spectrophotometer at room temperature. The optical absorption data is shown in Figure 3.3 as a function of photon energy. The black dashed lines represent the Urbach slope

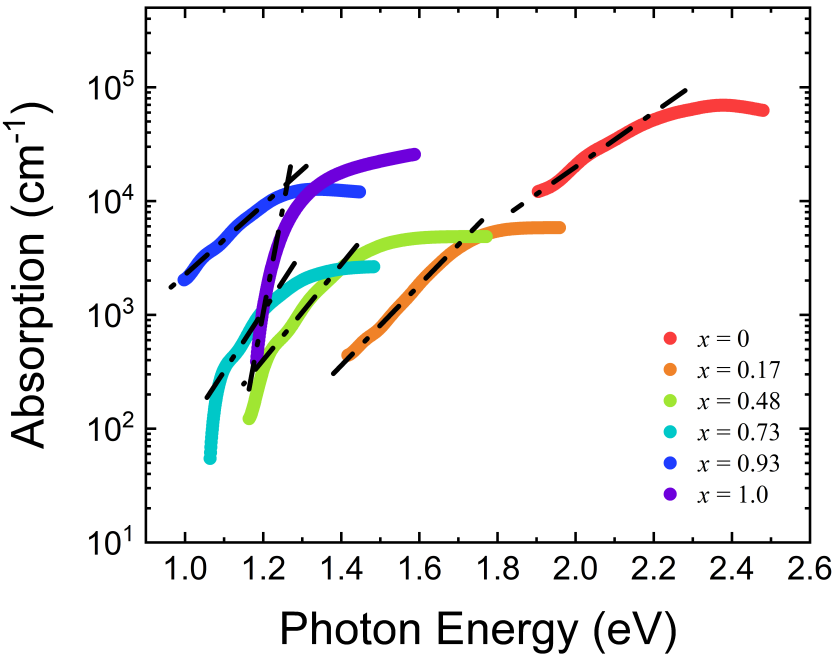

Figure 3.3: Absorption coefficient as function of photon energy obtained using a UV–Vis spectrometer for the a-$Si_{1-x}Ge_x$:H thin film series. Also shown (black lines) is their corresponding Urbach slope (E_U).

(E_U), related to T_o according to the convention $E_U = kT_o$. The resulting values of E_U and T_o are presented in Table 3.2 for each sample. The Urbach energy found is in the order of the tens of meV, regardless of Ge content.

Figure 3.4 shows the Tauc plot obtained from the absorption data of the samples under study. As discussed before in Section 2.3, we can extract the optical bandgap (E_{opt}) information from this plot. A summary of the resulting E_{opt} values is shown in Table 3.2.

The E_{opt} values show a monotonic decrease in the optical bandgap as the Ge content gets increased for the $0 \leq x \leq 0.93$ range. This behavior has been reported in several other studies [46, 49, 50]. Furthermore, the optical bandgap values for the a-Si:H and the 93% Ge film, which is comparable to an a-Ge:H sample, are in

Sample	E_U (meV)	T_o (K)	E_{opt} (eV)
a-Si:H	181.2	2102	1.70
a-$Si_{83}Ge_{17}$:H	122.8	1425	1.39
a-$Si_{52}Ge_{48}$:H	103.4	1200	1.12
a-$Si_{27}Ge_{73}$:H	23.5	273	0.99
a-Si_7Ge_{93}:H	141.3	1639	0.89
a-Ge:H	23.6	274	1.14

Table 3.2: Urbach energy (E_U), characteristic temperature (T_o), and optical bandgap energy (E_{opt}) of the a-$Si_{1-x}Ge_x$:H sample series.

agreement with reported values for a-Si:H and a-Ge:H, respectively.

However, the a-Ge:H sample does not follow this trend, showing a higher optical bandgap than the 48% Ge sample. We believe this is due to this film being much thinner in comparison to the rest of the series. Thinner films tend to have slightly different hydrogen content than films that are $\sim$ (1 – 2) μm thick. The H content has been proven to significantly shift the absorption edge of a-Ge:H samples to higher values as the H content is increased [51].

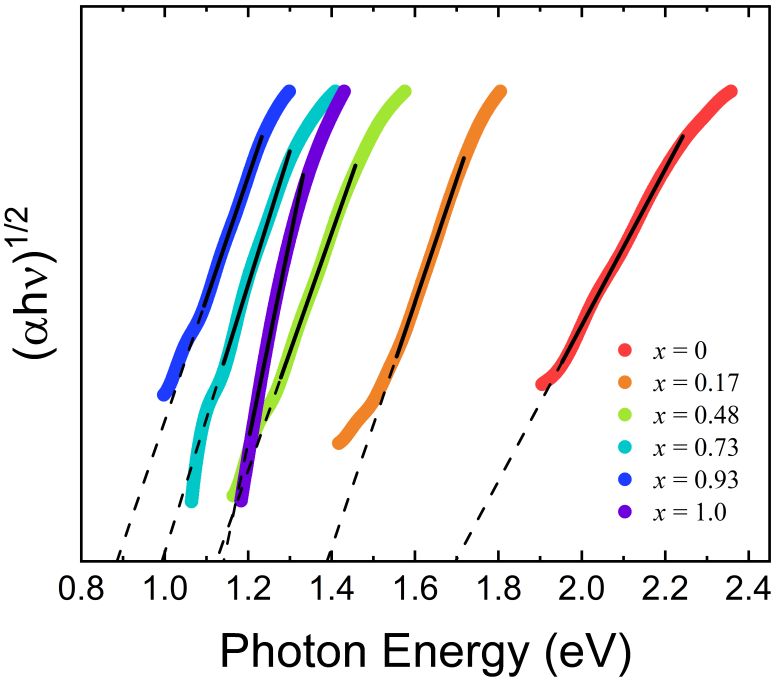

Figure 3.4: Tauc plot of the a-$Si_{1-x}Ge_x$:H thin film series. The $(\alpha h\nu)^{1/2}$ y–axis is shown as a.u. to allow all samples' data to be shown.

Chapter 4

Charge Transport Properties of a-$Si_{1-x}Ge_x$:H thin films

4.1 Conductivity

In thermally activated transport processes, the conductivity depends exponentially on the inverse of the temperature, as in Eq. (1.2). This expression can be rewritten as

$$\sigma(T) = \sigma_o \exp\left[-\left(\frac{E_\sigma}{k_B T}\right)\right], \tag{4.1}$$

where k_B is Boltzmann's constant, σ_o is the pre–exponential factor and $E_\sigma = \epsilon_{CB} - \epsilon_F$ is the activation energy, which represents the separation between the conduction band edge and the Fermi energy for n–type conduction. In a-Si:H, the conductivity pre–factor is $\sigma_o \sim 200$ $(\Omega\text{-cm})^{-1}$ [19, 52]. However, observed values of σ_o can vary by several orders of magnitude due to the Meyer–Neldel rule [51]. An Arrhenius plot of $\log(\sigma)$ against $1/k_B T$ would yield a straight line with slope equal to E_σ, the activation energy.

The dark conductivity corresponding to the a-$Si_{1-x}Ge_x$:H alloy films is presented in Figure 4.1. The conductivity can be fit reasonably well with a simple thermally activated expression over the range of 300 K to 470 K (Figure 4.1a), particularly for

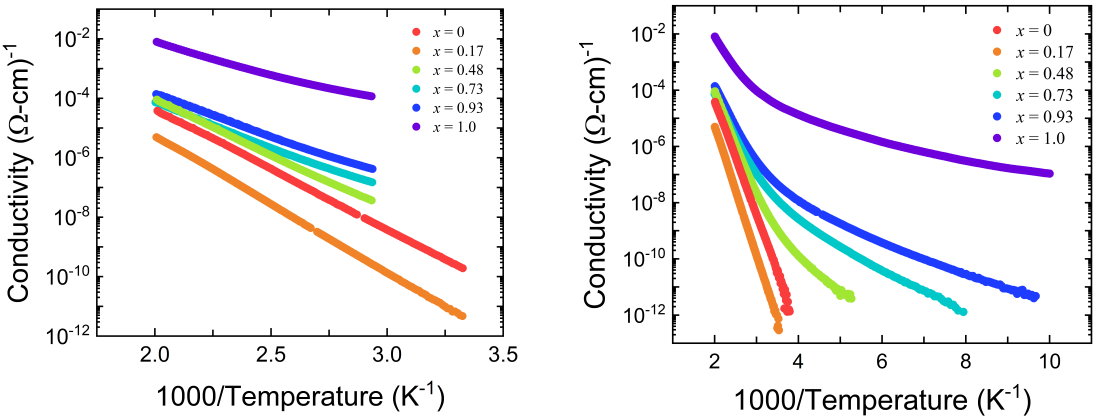

(a) (b)

Figure 4.1: Arrhenius plot of the dark conductivity of the a-$Si_{1-x}Ge_x$:H sample series for Ge content $0 \leq x \leq 1$. Films with $x \leq 0.17$ display a noticeably different conductivity behavior than films with $x \geq 0.48$.

films with lower Ge concentrations.

The activation energies and conductivity pre–exponential factors σ_o corresponding to Figure 4.1a are listed in Table 4.1. The activation energy increases for the film with Ge content of 17% when compared to the pure a-Si:H. For the samples with $x \geq 0.48$ the activation energy changes behavior and gradually decreases as the Ge content increases. The range of activation energies of the samples with $x \geq 0.48$ Ge content is less than those seen in both the a-Si:H and the a-$Si_{83}Ge_{17}$:H samples.

However, there are indications of deviations from an Arrhenius behavior, notably for films with germanium concentrations above 48%. When the data in Figure 4.1a is extended to lower temperatures, as shown in Figure 4.1b, clear non–Arrhenius behavior is observed.

Even for the pure a-Si:H and a-$Si_{83}Ge_{17}$:H films, which appear to be well–described by a simple thermally activated expression in Figure 4.1a, there is a slight curvature present in the measured values when compared to the expected value from an Arrhenius expression.

Sample	σ_o $(\Omega\text{-cm})^{-1}$	E_σ (eV)
a-Si:H	5.71×10^3	0.81
a-$Si_{83}Ge_{17}$:H	2.67×10^4	0.92
a-$Si_{52}Ge_{48}$:H	7.15×10^3	0.76
a-$Si_{27}Ge_{73}$:H	2.51×10^2	0.62
a-Si_7Ge_{93}:H	2.31×10^2	0.58
a-Ge:H	2.59×10^1	0.40

Table 4.1: Results of fits to an Arrhenius behavior (Eq. (4.1)) for the a-$Si_{1-x}Ge_x$:H sample series.

The temperature dependence of the dark conductivity is best determined by a log–log plot of the reduced activation energy (W) as function of temperature for the a-$Si_{1-x}Ge_x$:H series (Figure 4.2), known as a Zabrodskii analysis, explained in more detail in Section 1.1. From this figure it is clear that the a-Si:H and a-$Si_{83}Ge_{17}$:H samples are fundamentally different than those with $x \geq 48$ Ge concentration.

Figure 4.3 shows an expanded version of Figure 4.2 showing the a-Si:H and a-$Si_{83}Ge_{17}$:H samples. Overlaid on the plot are calculations of the reduced activation energy for conductivity temperature dependences of the form of Eq. (1.7) where $\kappa = 1$ (dashed green) and $\kappa = 1/2$ (dashed blue), as well as the line corresponding to the best fit (solid black). The conductivity temperature dependence is inconsistent with the $\kappa = 1$ and $\kappa = 1/2$ model curves and matches very closely the $\kappa = 3/4$ model curve found in previous studies [18, 53]. The best fits for the a-Si:H and a-$Si_{83}Ge_{17}$:H samples requires a power exponent of $\kappa = 0.72$ and $\kappa = 0.79$, with T_o values of 4.5 eV and 3.0 eV, and $\sigma_1 = 1.0 \times 10^8$ $(\Omega\text{-cm})^{-1}$ and 3.9×10^7 $(\Omega\text{-cm})^{-1}$, respectively. These are consistent with anomalous hopping measurements of a-Si:H reported previously [18].

To look further into the $\kappa = 0.79$ relationship, Figure 4.4a shows the data for the

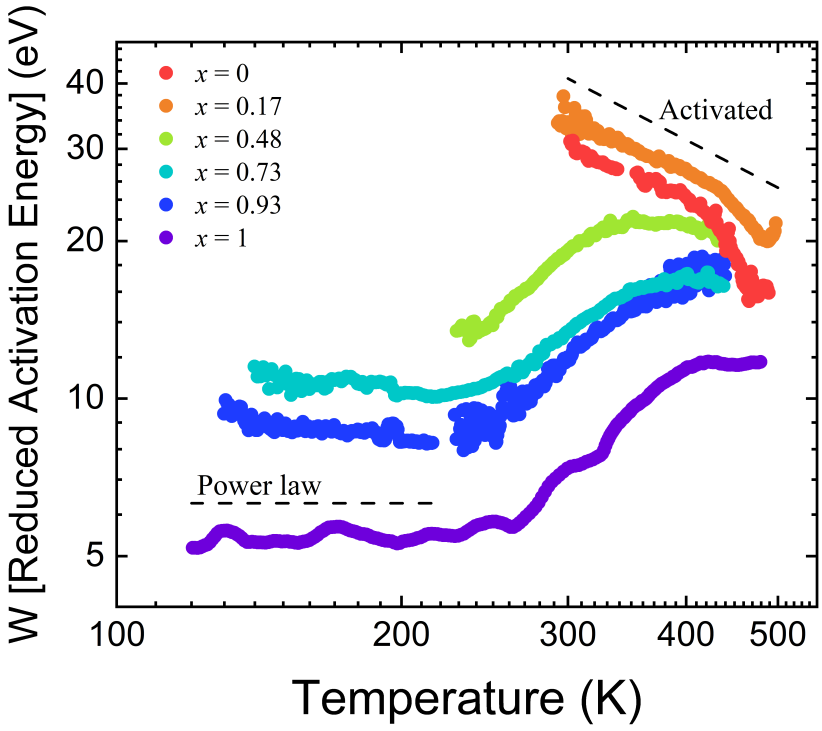

Figure 4.2: Log–log plot of the reduced activation energy (W) vs temperature for the a-$Si_{1-x}Ge_x$:H series with $x \geq 0.48$. The data forms a horizontal line at low temperatures, suggesting a power–law relationship.

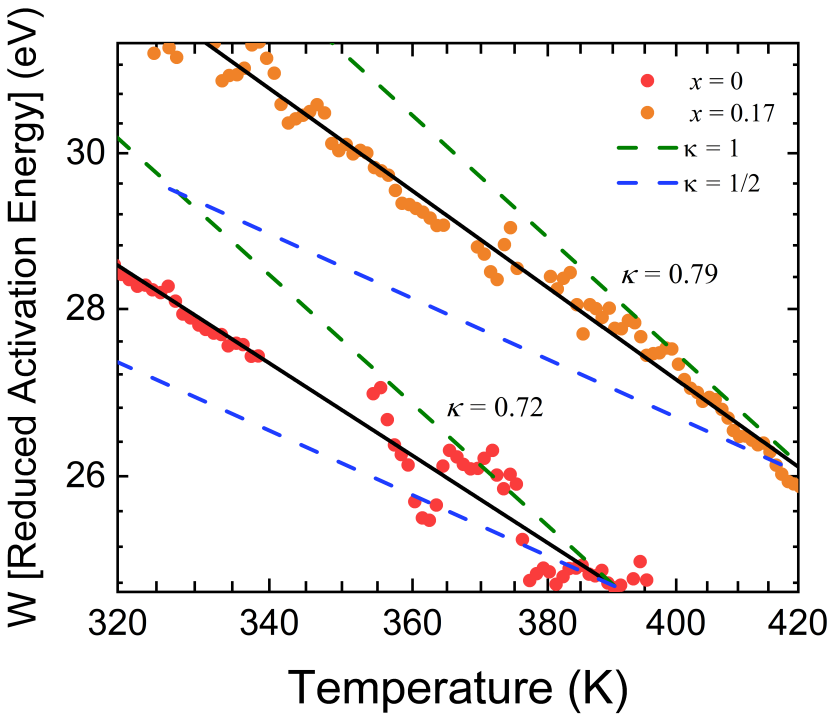

Figure 4.3: Log–log plot of the reduced activation energy (W) vs temperature for the a-Si:H and a-$Si_{83}Ge_{17}$:H samples. Overlaid on the plot are model curves of the form of Eq. (1.7), with $\kappa = 1$ (dashed green), $\kappa = 1/2$ (dashed blue), and the κ values that correspond to each samples' best fit lines (solid black).

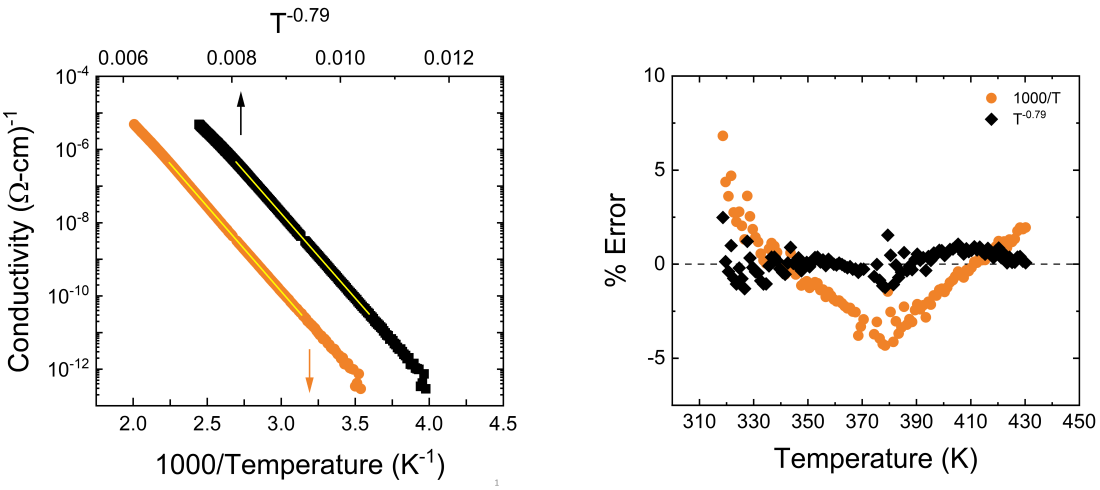

(a) (b)

Figure 4.4: (a) Plot of the temperature dependent conductivity of the a-$Si_{83}Ge_{17}$:H film when plotted against T^{-1} (orange circles) and $T^{-0.79}$ (black diamonds). The best fit lines (yellow) are overlaid on the data. (b) Plot of deviation percentages from fits of Eq. (4.1) (orange circles) and Eq. (1.7) with $\kappa = 0.79$ (black diamonds) corresponding to the data in Figure 4.4a.

a-$Si_{83}Ge_{17}$:H film, also shown in Figure 4.1, now plotted on both an Arrhenius plot (orange circles) and against $T^{-0.79}$ (black diamonds). Note that in this plot $\kappa = 0.79$ is not an adjustable parameter, but rather the value determined from the Zabrdoskii analysis (Figure 4.3). The yellow lines overlaying the data in Figure 4.4a are both straight lines. However, the plot vs $1000/T$ shows a slight curvature over the entire temperature range, while the plot vs $T^{-0.79}$ shows no detectable curvature. A simple estimation of the Joule heating experienced by these samples at low temperatures suggests a temperature increase of the order of 1 mK, which is insufficient to account for the curvature in Figure 4.4a. A plot of the percent difference between the data and the best fit line for fits to $1000/T$ and $T^{-0.79}$ conductivity dependence, Figure 4.4b, indicates that the latter provides a more accurate description of the data. A similar result is achieved when analyzing the a-Si:H sample in the same manner.

As mentioned above, Figure 4.2 indicates a distinct transition in the dark conductivity temperature dependence at $x = 0.48$. For those samples, two different behaviors at high and low temperatures become apparent. The behavior at low temperatures is best described by a horizontal line in Figure 4.2, suggesting a power–law relationship between the conductivity and the temperature, that is

$$\sigma(T) = \sigma_o^* \left(\frac{T}{T_o^*} \right)^n . \tag{4.2}$$

Indeed, when the conductivity data σ is plotted on a log–log plot against T for the low temperature regime, as shown in Figure 4.5, an excellent fit is obtained. A linear fit on the log–log plot, shown in yellow, is consistent with the data, validating the power–law relationship. This behavior has been observed in non–hydrogenated a-Ge,[54] as well as amorphous carbon [53, 55], metal–oxide glasses [14, 56], and grain boundary states in nanocrystalline diamond [57], and is most often ascribed to Multi–Phonon Hopping (MPH). A deeper consideration of an MPH–type conduction modeling will be discussed in Section 5.1.

Table 4.2 shows the values of n resulting from the fit to the data in Figure 4.5 at low temperatures, exhibiting a decreasing trend of the n value as the Ge content increases. Note that these power–law exponents are consistent with the horizontal intercepts of the plot of Reduced Activation energy against temperature (Figure 4.2).

Previous studies of non–hydrogenated a-Ge and a-SiGe have observed deviations from Arrhenius behavior, with charge transport at lower temperature dependencies being attributed to a VRH mechanism, where the conductivity varies as Eq. (1.7) with $\kappa = 1/4$ [58, 59], and for very low temperatures, to ES–VRH, where κ takes the value of 1/2 [59]. A comparison between different temperature dependences of the a-Ge:H dark conductivity is presented in Figure 4.6a, including those corresponding to Mott–VRH and ES–VRH. Specifically, the comparison shows the conductivity data as function of $1000/T$, $T^{-1/2}$, $\log(T)$, and $T^{-1/4}$ for the low temperature range.

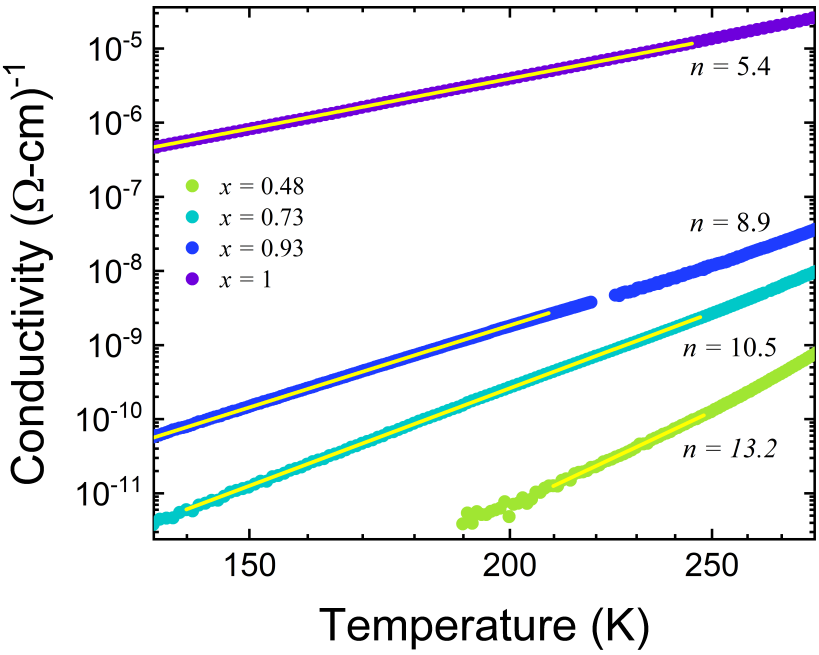

Figure 4.5: Log–log plot of the dark conductivity vs temperature for the a-$Si_{1-x}Ge_x$:H series with $x \geq 0.48$ for the low temperature range. The linear behavior is consistent with an MPH type of conduction.

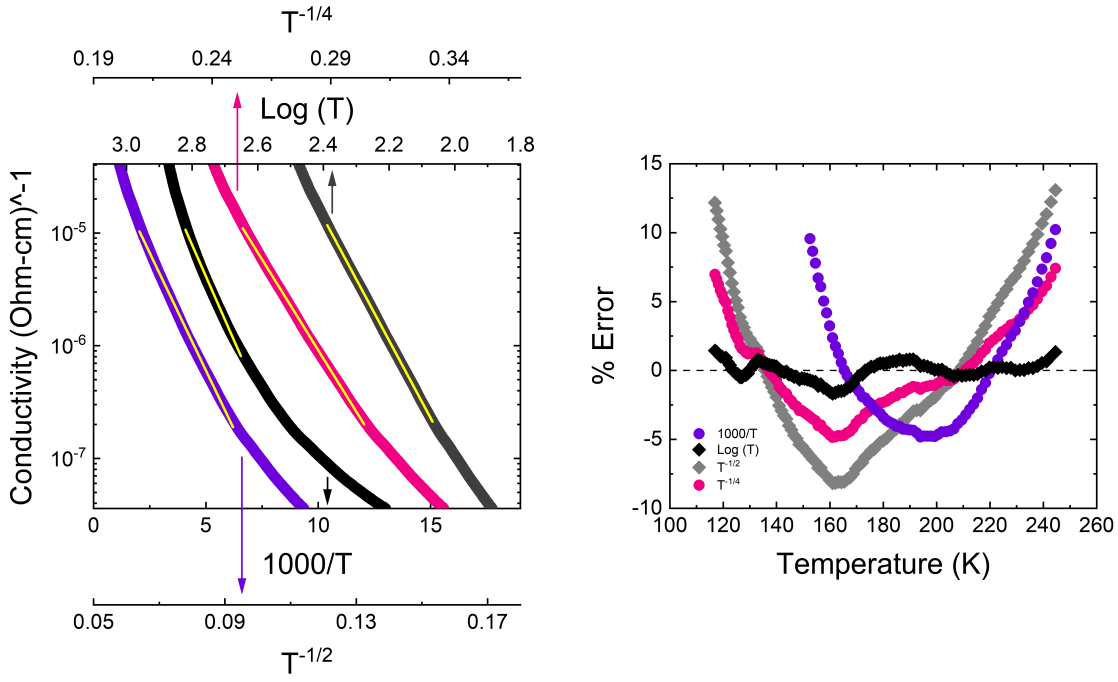

(a) (b)

Figure 4.6: (a) Plot of the log of the dark conductivity of the a-Ge:H film when plotted against $1000/T$ (purple circles), $T^{-1/2}$ (gray diamonds), $\log(T)$ (black diamonds), and $T^{-1/4}$ (pink circles). The best fit lines (yellow) of each are overlaid on the data. (b) Plot of the percent differences from fits of Eq. (4.1) (purple circles), Eq. (1.7) with $\kappa = 1/2$ (gray diamonds), Eq. (4.2) (black diamonds), and Eq. (1.7) with $\kappa = 1/4$ (pink circles), corresponding to the data in (a), respectively.

Sample	n values
a-$Si_{52}Ge_{48}$:H	13.7
a-$Si_{27}Ge_{73}$:H	10.5
a-$Si_{7}Ge_{93}$:H	8.9
a-Ge:H	5.4

Table 4.2: Resulting n values from fits of the form of Eq. (4.2) at low temperatures for the a-$Si_{1-x}Ge_x$:H samples with $x \geq 0.48$.

Figure 4.6a clearly shows that the Arrhenius ($1000/T$) and the ES–VRH ($T^{-1/2}$) relationships do not adequately describe the dark conductivity of the a-Ge:H sample, as the data shows curvature when compared to their respective best fit lines (yellow). When plotted as $\log(\sigma)$ against $T^{-1/4}$ there is a reasonable fit to the data for a temperature range comparable to that of the power–law fit. However, as shown in Figure 4.6b, the percent error for the VRH expression is significantly larger than for the power–law temperature dependence.

The highest temperature employed in the conductivity studies is < 500 K, which is deliberately kept below the deposition temperature of 520 K in order to avoid irreversible changes in the structural and electronic properties of the samples. Consequently, the range over which the temperature is varied is limited and alloys with a Ge concentration of $x \geq 0.48$ exhibit a Reduced Activation Energy consistent with either $\kappa = 3/4$, as that shown in the a-Si:H and a-$Si_{83}Ge_{17}$:H samples, or $\kappa = 1$.

4.2 Photoconductivity

As described in Section 1.2, pure a-Si:H thin films exhibit a dramatic increase in conductivity when exposed to light. Illumination causes an increase in the conductivity by several orders of magnitude as a result of the generation of electron–hole

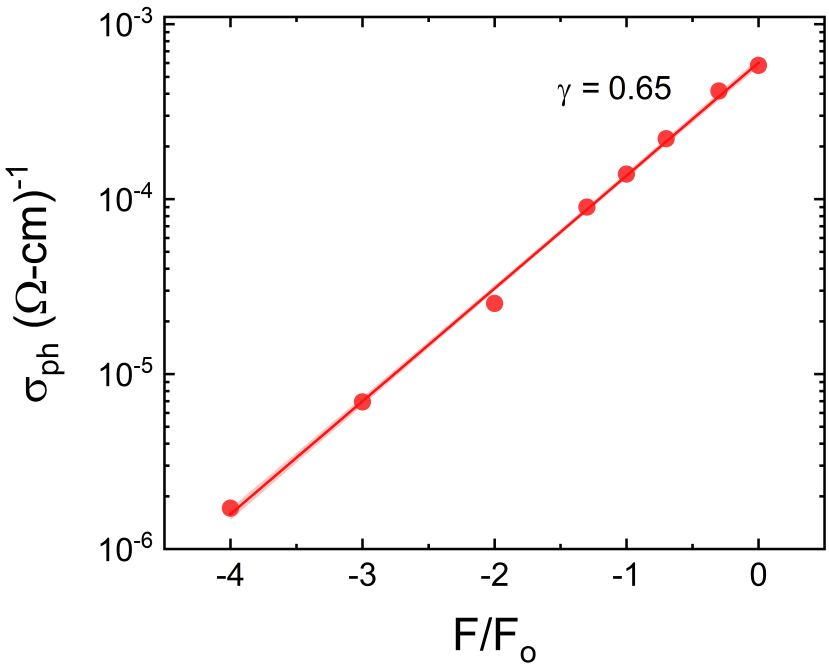

Figure 4.7: Log–log plot of the photoconductivity σ_{ph} vs the ration of irradiated light for the a-Si:H thin film. The slope of the linear function represents the exponent γ in Eq. (1.10).

pairs following the absorption of photons with energies larger than the film's bandgap. This section discusses the generation of the light–induced enhanced conductivity in the a-$Si_{1-x}Ge_x$:H film series as function of light intensity.

Prior to photoconductivity measurements the sample is annealed at 470 K for two hours (state A) to remove any previous light–induced defects. Figure 4.7 shows the effective photoconductivity $\sigma_{ph} = \sigma_m - \sigma_A$ as a function of light intensity in a log–log plot for the pure a-Si:H sample. This relationship is governed by (Eq. (1.10)), with the slope equal to the exponent γ. Similar plots were constructed for the samples in the a-$Si_{1-x}Ge_x$:H film series, and γ values were determiend. A plot of the resulting γ values as function of Ge content is shown in Figure 4.8.

In Section 1.2 we mentioned that a γ value between 0.5 and 1 comes as a con-

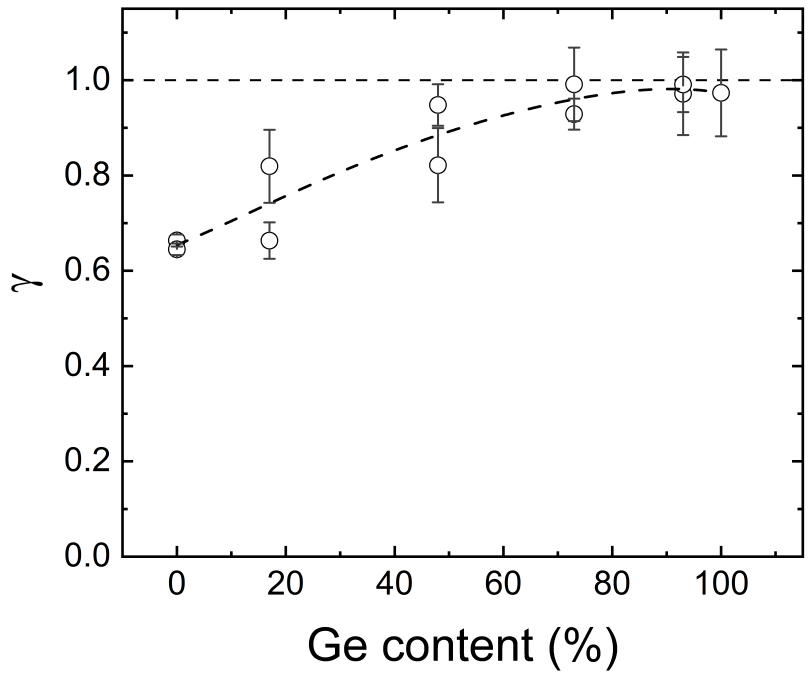

Figure 4.8: Plot of the Eq. (1.10) exponent γ as function of the Ge content for the a-$Si_{1-x}Ge_x$:H thin film series.

sequence of the continuous nature of the density of states. This is the case for our samples, which range between 0.6 and 1, and increase as a function of the Ge content. Samples with higher Ge content have an exponent close to unity, indicating a nearly linear dependence of the photoconductivity with the light power density. This transition from bimolecular to monomolecular recombination would indicate an increasing role of mid–gap defects on the recombination process with increasing germanium content.

The photoconductivity value carries information on the density of recombination centers in a sample, typically ascribed to dangling bond defects. The higher the density of dangling bonds, the lower the photoconductivity of a sample, as more photo–excited electrons are trapped in the defects. Figure 4.9 shows the measured photoconductivities σ_{ph} for the a-$Si_{1-x}Ge_x$:H film series taken at room temperature for a fixed light intensity. The decrease in σ_{ph} between the a-Si:H and a-Ge:H samples is attributed to the preference of H atoms to bond with Si rather than Ge, resulting in a large defect density from the unhydrogenated Ge atoms [60, 61]. Samples in the low to mid–range of Ge content show the lowest photoconductivity. This is most likely due to the presence of both Si and Ge dangling bonds in higher concentrations than in the pure a-Si:H and a-Ge:H samples.

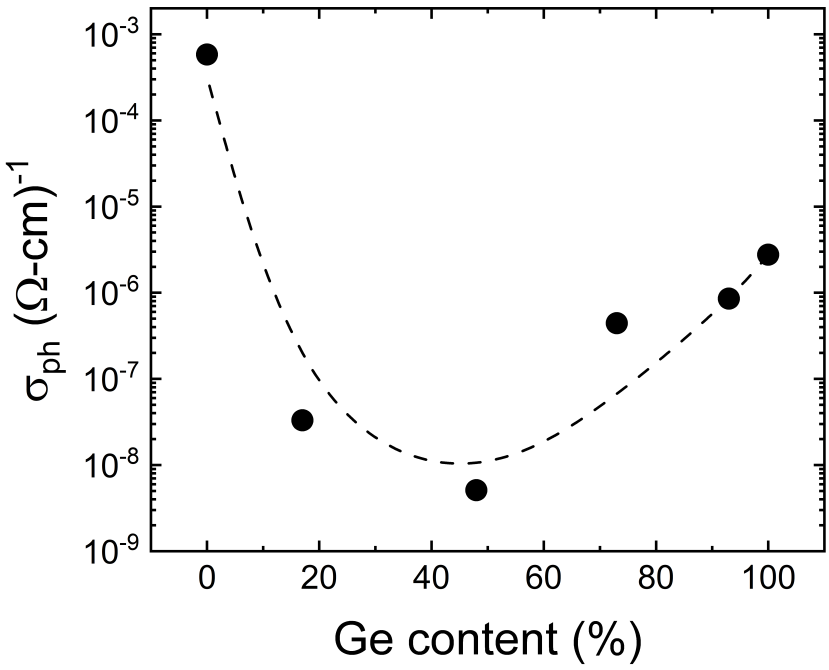

Figure 4.9: Plot of the photoconductivty of the a-$Si_{1-x}Ge_x$:H thin film series at room temperature as function of Ge content. The dashed line serves as a visual guide.

4.3 Thermopower

The thermopower of the a-$Si_{1-x}Ge_x$:H thin–film samples was measured using the system and procedure described in Section 2.4.3. Figure 4.10a shows the raw thermopower data for a pure a-Si:H sample in a ΔV vs T plot. Each group of data points, connected by a line, represents a different average T, ranging form 310 K to 480 K, and each data point within a group corresponds to a different ΔT. All curves clearly display a negative slope over the entire temperature range examined, indicating n–type conduction. Similarly, a film with $x = 0.48$, shown in Figure 4.10b, displays an induced voltage against temperature with a positive slope, indicating p–type conduction. In contrast, a film with $x = 0.73$, shown in Figure 4.10c, displays a negative slope near room temperature, while above $\sim$ 380 K the slope switches to a positive value. This measurement procedure was repeated for all of the synthesized films, with $0 < x < 1$, and was observed in other alloy films with the same Ge concentrations.

Figure 4.11 shows measured values of the Seebeck coefficient (Eq. (4.3)) as a function of temperature in the (310 – 480) K range for all films studied here. The sign of the Seebeck coefficient contains information about the type of conduction taking place, i.e. p–type or n–type. Although a-Si:H and a-Ge:H show an n–type conduction, this is not seen for all the alloy films. As the Ge content is increased to 17%, the sample still maintains its n–type nature. However, the 48% Ge sample shows positive Seebeck coefficient values for all measured temperatures; and a switch from negative to positive Seebeck coefficient is seen in the 73% Ge sample as function of temperature. Samples with higher Ge content ($x \geq 0.93$) return to a negative Seebeck coefficient.

By fitting the data shown in Figure 4.11 to the expression:

$$S = \frac{k_B}{e}\left[\frac{E_S}{k_B T} + A\right], \tag{4.3}$$

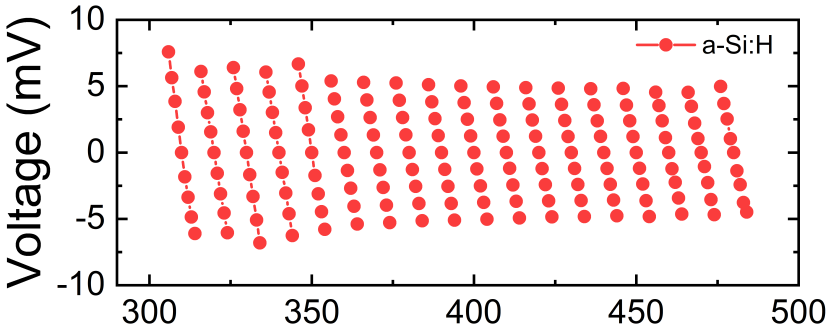

(a)

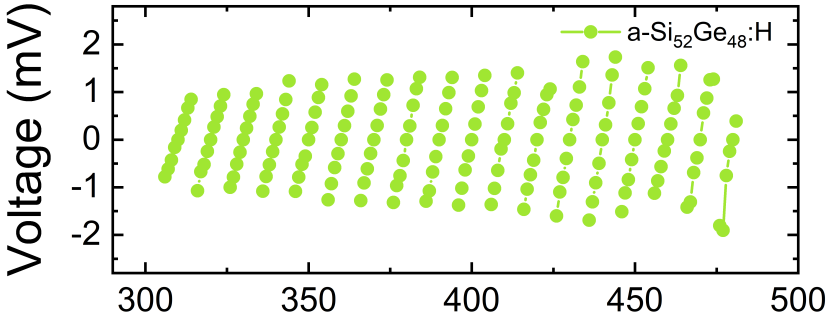

(b)

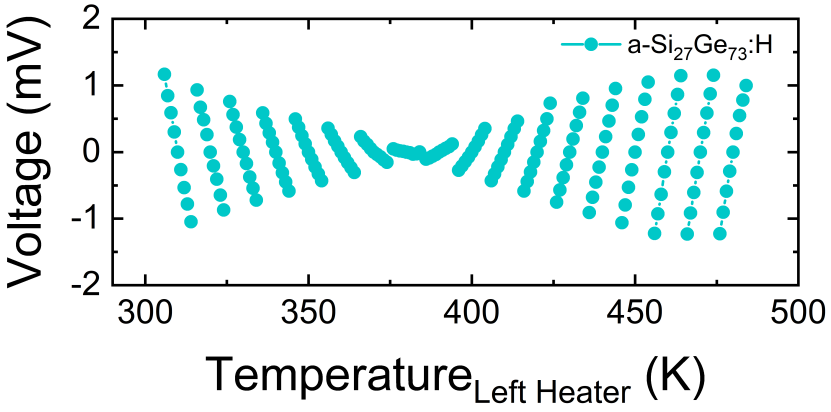

(c)

Figure 4.10: Plots of measured voltage vs temperature for three samples with (a) $x = 0$, (b) $x = 0.48$, and (c) $x = 0.73$. Each curve on the plots represents the voltage measurements at temperatures $T = T_{avg} \pm \Delta T/2$ and $T = T_{avg}$. A negative slope indicates n–type conduction, while a positive slope indicates p–type conduction.

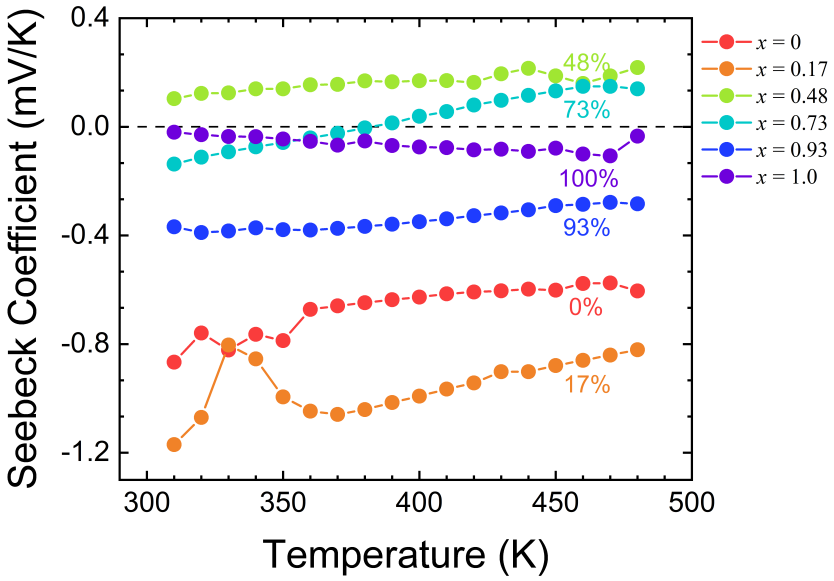

Figure 4.11: Seebeck coefficient as function of temperature for the a-$Si_{1-x}Ge_x$:H series. The average temperature ranges from (310 – 480) K. A switch in the Seebeck coefficient sign is seen as function of temperature and Ge content.

it is possible to determine the activation energy E_S. Table 4.3 shows a summary of the activation energies for all samples. These show a negative sign for all samples, except the purely a-Ge:H. The activation energy obtained from the temperature dependence of the dark conductivity, also shown in Table 4.3, is larger by up to several hundred meV than that determined from the measured Seebeck coefficient, a feature of all amorphous semiconductors. This difference in activation energy has been ascribed to the influence of long–ranged disorder, arising from potential fluctuations or compositional modulations, on charge transport [48, 62]. As discussed in the next section, the fact that the dark conductivity in the a-$Si_{1-x}Ge_x$:H films is not well described by the conventional excitation of charges to extended states above the Mott–mobility edge raises doubts about this interpretation of the activation energy difference.

Sample	E_σ	E_S
a-Si:H	0.81	-0.14
a-$Si_{83}Ge_{17}$:H	0.92	-0.39
a-$Si_{52}Ge_{48}$:H	0.76	-0.09
a-$Si_{27}Ge_{73}$:H	0.62	-0.31
a-Si_7Ge_{93}:H	0.58	-0.15
a-Ge:H	0.40	0.07

Table 4.3: Comparison between the dark conductivity activation energy E_σ (eV) at high temperatures, assuming an Arrhenius behavior, and the Seebeck activation energies E_S (eV) for the a-$Si_{1-x}Ge_x$:H sample series.

Chapter 5

Discussion of Results

This chapter considers the dark conductivity and Seebeck coefficient measurements of the a-$Si_{1-x}Ge_x$:H films presented in Chapter 4. While the previous discussion described our results in the context of understanding the influence of varying the Si/Ge ratio, this section focuses on arriving to a fuller understanding of the transport properties of these films.

5.1 Dark conductivity

As discussed in Section 4.1, alloys with Ge content $x \geq 0.48$ show a Zabrodskii analysis Reduced Activation Energy slope equal to zero at temperatures below 250 K, as shown in Figure 4.2. This slope is characteristic of a power–law temperature dependent conductivity, typically connected to an MPH conduction through localized states, such as dangling bonds.

In the standard description of MPH,[23, 24, 29], charges reside in the weakly localized defect states, and preferentially couple to phonons with wavelengths comparable to the defect's localization length. For Ge dangling bond defects, this localization length would be on the order of 1.1 nm [63]. The hopping process therefore involves long–wavelength low–energy acoustic phonons, and consequently multiple phonons

must participate in a single hop event.

The hopping conductivity is given by the expression [17]:

$$\sigma_{MPH} = \frac{(eR)^2 N_c}{6k_B T}\Gamma, \tag{5.1}$$

where N_c is the density of localized carriers (equivalent to the number of occupied defect states), e is the electron charge, k_B is the Boltzmann constant, T is the temperaure, R is the hopping distance and Γ is the hopping rate.

If p phonons are required to initiate a transition from one defect state to another, then the hopping frequency depends on p factors of the Bose–Einstein distribution function. The rate Γ has been determined by Robertson and Friedman [52, 64], and can be expressed as:

$$\Gamma = \nu_o \exp\left[-\frac{2R}{\alpha}\right] \exp\left[-\frac{E_M}{h\nu_o}\right] \left(\frac{E_M}{h\nu_o}\right)^p [n_{BE}(\nu_o)]^p, \tag{5.2}$$

where α is the localization radius, E_M is a measure of the electron–phonon coupling, $n_{BE}(\nu_o)$ is the Bose–Einstein distribution for phonons of frequency ν_o, and p is the number of phonons needed for the hopping to take place. In the regime of $h\nu_o \ll k_B T$ the Bose–Einstein distribution factor in Eq. (5.2) can be Taylor expanded into a power–law of the form of Eq. (4.2), with $n = p - 1$.

The low temperature range of all samples with $x \geq 0.48$ was fitted using equations Eq. (5.1) and Eq. (5.2), indicated by the dashed lines overlaid with the data in Figure 5.1. This plot is similar to that shown in Figure 4.5, except the fitting in this case corresponds to the exact expression describing the conductivity, rather than an approximation. The factors ν_o and E_M are kept as free parameters given that we do not possess a procedure to accurately estimate them. The rest of the parameters were determined using literature values or from past measurements. From the photoconductivity measurements shown in Section 4.2 we are able to estimate the density of defects. In MPH, transport is assumed to take place through defect states; therefore,

we can use the dangling bond density for N_c. The hopping distance between states R was estimated as $R = 1/N_c^{1/3}$. From the power–law fittings shown in Figure 4.5 we can determine $p = n + 1$. The localization radius α of dangling bond defects in a-Si:H and a-Ge:H has been found to be 0.5 and 1.1 nm [63], respectively. We can then interpolate the corresponding values for samples with $0.48 \leq x \leq 0.93$. For this, we use a non–monotonic interpolating function determined by Street and co–workers [49] for a-$Si_{1-x}Ge_x$:H samples. In ref. [49] the authors determined the distance between an electron–hole pair and the nearest dangling bond (critical transfer radius) R_c as a function of their Ge concentration. R_c is expected to be proportional to α, so we can used this relationship for the interpolation. The fixed and resulting fitting parameters ν_o and E_M used for the modeling of the dark conductivity data are shown in Table 5.1.

Sample	N_c (cm^{-3})	R (cm)	α (cm)	p	E_M (meV)	ν_o (GHz)
a-$Si_{52}Ge_{48}$:H	1.1×10^{21}	1.2×10^{-7}	2.6×10^{-8}	14.2	74	131
a-$Si_{27}Ge_{73}$:H	1.3×10^{19}	7.0×10^{-8}	6.4×10^{-8}	11.5	48	103
a-Si_7Ge_{93}:H	6.8×10^{18}	5.1×10^{-7}	9.7×10^{-8}	9.9	9.5	22.0
a-Ge:H	2.1×10^{18}	9.6×10^{-7}	11×10^{-8}	6.4	9.2	47.9

Table 5.1: Parameters used and obtained from fitting the conductivity data to an MPH model. The density of carriers is given by N_c, calculated from the defect density resulting from photoconductivity measurements. R is set to $R = 1/N^{1/3}$. The localization radius α was obtained from an interpolation between reported values for a-Si:H and a-Ge:H.

The resulting E_M values are between (8 – 60) meV, and scale inversely to the Ge content of the samples. These values are consistent with those found through density–functional calculations by Drabold et.al. [65, 66] in an a-Si model consisting of 216 atoms. In the study, by computing the sensitivity of specific electronic eigenstates to

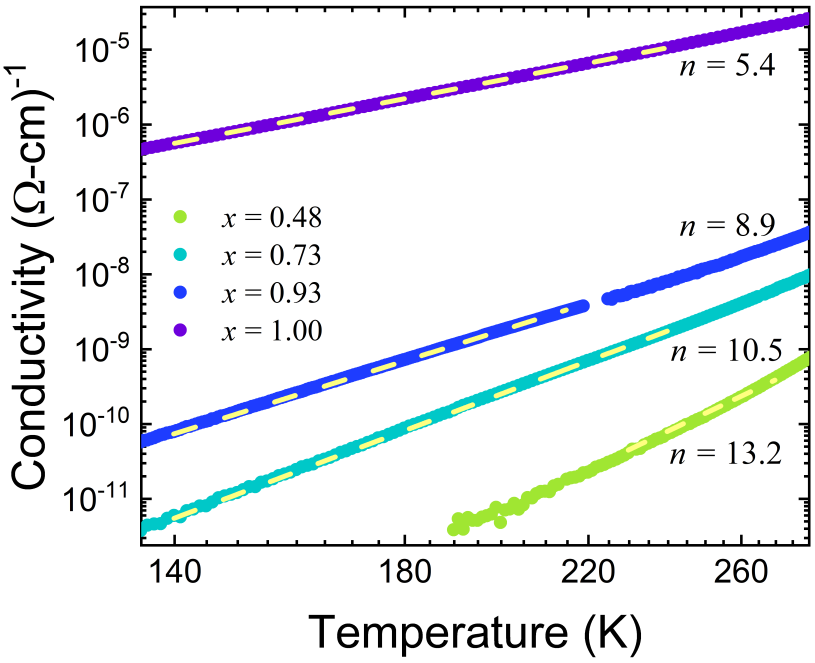

Figure 5.1: Log–log plot of the dark conductivity vs temperature for the a-$Si_{1-x}Ge_x$:H series with $x \geq 0.48$ in the low temperature range. The linear behavior is consistent with a MPH type of conduction, in which case the slope value n is related with the average number of phonons involved in the hopping process. The dashed yellow lines are fits to an MPH model as described in the text.

individual classical normal modes of vibration, the authors were able to show that localized states exhibit large electron–phonon coupling. The parameter ν_o was found to be on the order of ~ 0.1 THz for all the samples, which corresponds to a phonon temperature of ~ 5 K. This value of phonon frequency agrees with Shimakawa's estimation for MPH transport through dangling bonds in unhydrogenated a-Ge [54].

At temperatures at and above room temperature the MPH expression is unable to account for the observed conductivity temperature dependence, as previously discussed. However, when the expression in Eq. (5.1), using Eq. (5.2) for Γ and the parameters from Table 5.1, is combined with an anomalous hopping conduction at high temperatures, described by Eq. (1.7), the resulting expression provides a satisfactory fit to the data over the entire temperature range investigated, as indicated by the dashed lines in Figure 5.2.

The Zabrodskii analysis (Figure 4.2) is ambiguous as to whether anomalous hopping or simple thermally activated conduction dominates at high temperatures. Through a comparison between the percent error corresponding to an anomalous hopping and a simple Arrhenius expression fits at high temperatures (shown in Figure 5.3), it is evident that the $x = 0.48$ film's data is best described by anomalous hopping, while the fitting to the observed data for the $x \geq 0.73$ films are comparable for either expression.

Using a model of MPH conductivity at low temperatures combined with anomalous hopping at high temperatures, the fractional conductivity due to each transport mechanism is computed as a function of temperature. We can define the fractional conductivity as σ_i/σ_{tot}, where i is either the contribution to the conductivity due to anomalous hopping or MPH conduction. The resulting figure is shown in Figure 5.4. For all of the samples, there is a considerable contribution from MPH even at temperatures as high as 400 K. This is indicative of the existence of conduction through dangling defects in all samples, even for temperatures above room temperature. The

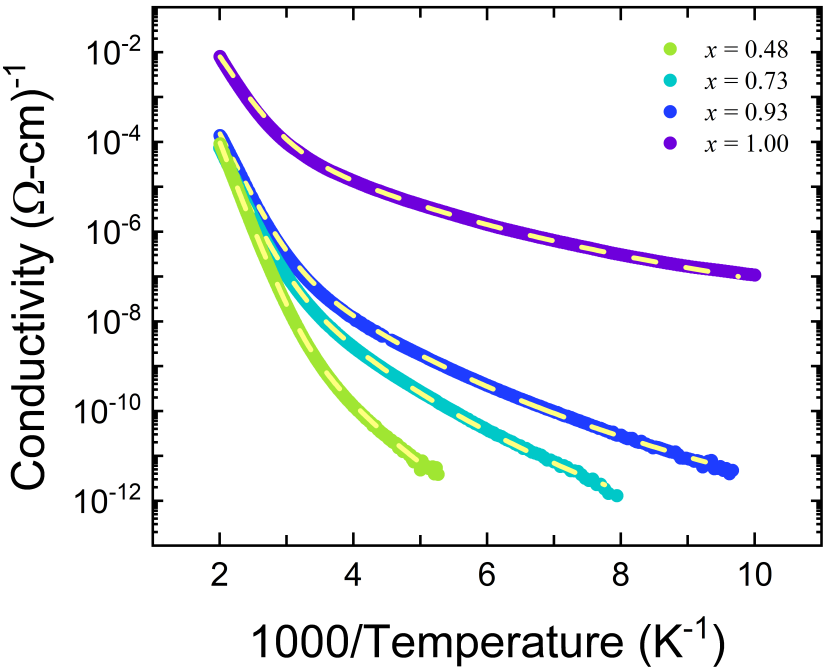

Figure 5.2: Arrhenius plot of the dark conductivity of the a-$Si_{1-x}Ge_x$:H sample series for Ge content $0.48 \leq x \leq 1.0$ for the full range of measured temperatures. The dashed yellow lines represent fits using the Anomalous Hopping and Multi–Phonon Hopping expressions, as described in the text.

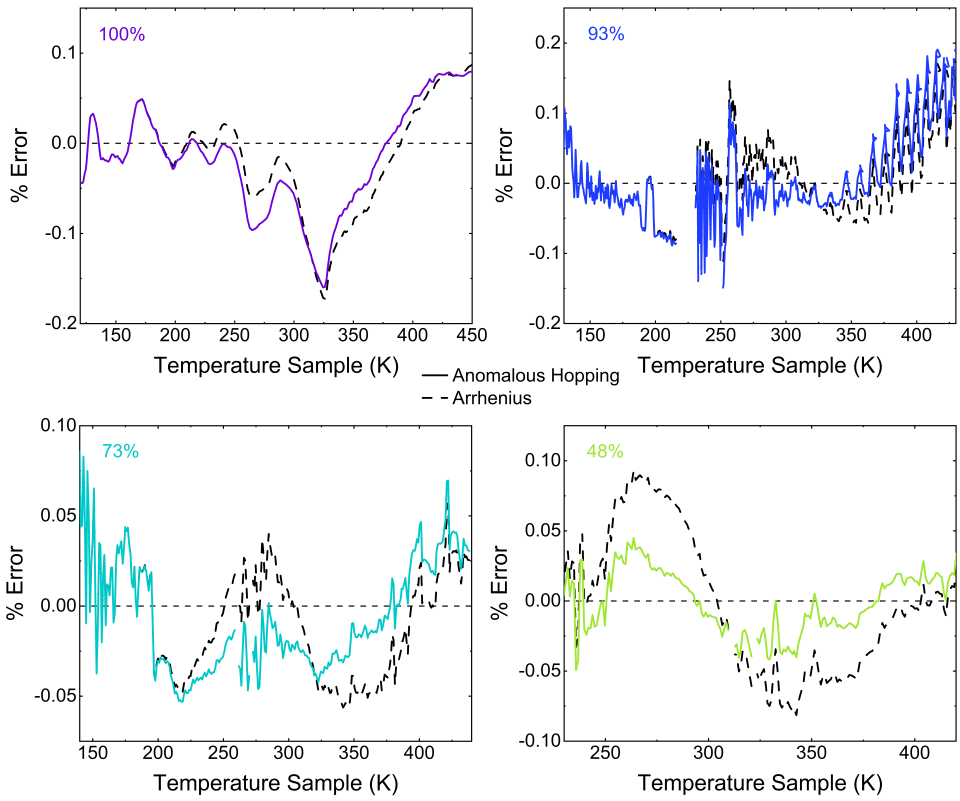

Figure 5.3: Comparison between the percent differences corresponding to fits to an anomalous hopping and an Arrhenius expression for the a-$Si_{1-x}Ge_x$:H sample series with $0.48 \leq x \leq 1.0$ Ge content.

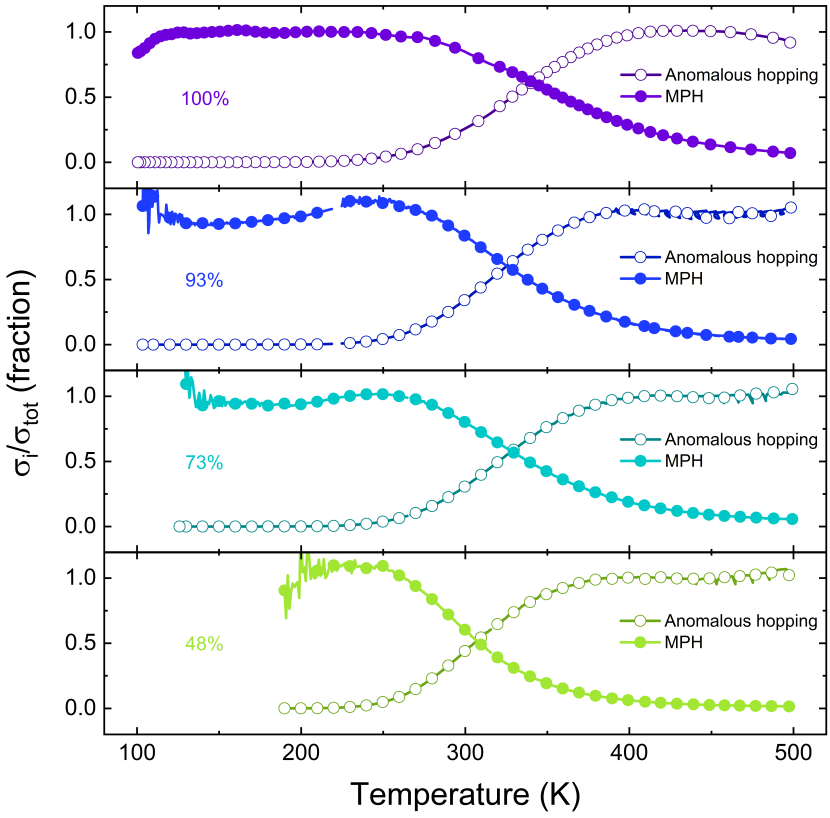

Figure 5.4: Calculated fractional conductivity, σ_i/σ_{tot} for each electronic transport mechanism (anomalous hopping and MPH) plotted against temperature for (100 – 500) K. All samples show a mix of conduction mechanisms even for temperatures as high as 400 K. Only every fifth data point has been displayed for clarity.

temperature at which the transition between conduction mechanisms happens (MPH to anomalous hopping), generally shifts to higher temperatures as the germanium content increases.

We are unaware of any published reports of MPH conduction at such high temperatures, with nearly all cases of MPH being observed below room temperature. At higher temperatures optical phonons with higher energies should be present, obviating the need for a multi–phonon process. In addition to that, our analysis indicates that

for some samples as many as fourteen phonons are required in order to hop between states. We believe it is possible that the observed power–law temperature dependence may indicate a different conduction mechanism, distinct from MPH. However, we do not have any suggestions for what this mechanism might be at this time.

5.2 Seebeck coefficient

Thermopower measurements of the a-$Si_{1-x}Ge_x$:H sample series show a transition from negative to positive Seebeck coefficient as a function of Ge content and temperature, as described in Section 4.3. The Fermi energy for these samples, as seen from the electrical dark conductivity analysis, resides in a continuous DOS where according to the MPH model, charge transport takes place. The Seebeck coefficient in such cases is better described using the expression for the thermopower of a metal, given by [67]:

$$S = \frac{k_B^2}{e} T \left. \frac{d \ln \mathrm{DOS}(E)}{dE} \right|_{E=E_f}, \tag{5.3}$$

where k_B is the Boltzmann constant, T is the temperature, e is the electron charge, $\mathrm{DOS}(E)$ is the density of states, and E_f is the Fermi energy. Here, the Seebeck coefficient is directly proportional to the derivative of the DOS at the Fermi level. Therefore, a change in the Seebeck coefficient sign may be interpreted as the result of the Fermi level moving within the mid–gap populated by dangling bond states, rather than due to a change in the carrier type of a band–to–band transport.

A previous study done by W. Paul and co–workers [50] looked at the photoconductivity and optical absorption properties of a-SiGe:H alloy samples, and argued that they could be explained through the combination of several factors. These were: the preferential attachment of H to Si dangling bonds, which leave many Ge based defects; the strongly overlapping of band tails, giving a high minimum gap DOS; and

the existence of different DOS involving Si and Ge dangling bond states at different energies, which result in charged defects that easily trap carriers for most positions of the Fermi level. All of these factors contributed to the postulation of a band structure for an a-$Si_{50}Ge_{50}$:H film.

Using Paul's proposed band structure we have sketched a plausible DOS for an alloy film with Ge content $\sim 70\%$ (Figure 5.5), where D_o and D^- correspond to the singly occupied (neutral) and doubly occupied (negative) localized dangling bonds, respectively. The dangling bonds' energy levels are different due to the electron–electron interaction, and therefore material dependent. They are characterized by the effective correlation energy (U_{eff}) which is the net energy necessary to transfer charge.

The 70% Ge sample shows a positive slope at the Fermi level, which is directly proportional to the Seebeck coefficient value (Eq. (5.3)), resulting in a positive S value. Then, if the DOS slope at E_f is positive (negative), we get a positive (negative) Seebeck coefficient. Now, if we either change the Ge content or the temperature of the sample, the Fermi energy level will move to a new position due to a statistical shift. If this new position results in a different sign for the slope of the DOS at E_f, we obtain a positive (negative) Seebeck coefficient as a result.

There is no reason to believe that a change in carrier type is present in our samples as function of Ge content or temperature. Rather, a Fermi level shifting through dangling bond defects seems to be the more plausible explanation. This is further supported by our dark conductivity and fractional conductivity analysis shown in Figure 5.4, which indicates that conduction in these films occurs, to a large extent, through the dangling bonds.

According to our dark conductivity model describing our a-$Si_{1-x}Ge_x$:H films for $x \geq 0.48$, the transport mechanism can be described as a dual–channel system, with two parallel temperature–variable resistors, one related to anomalous hopping and

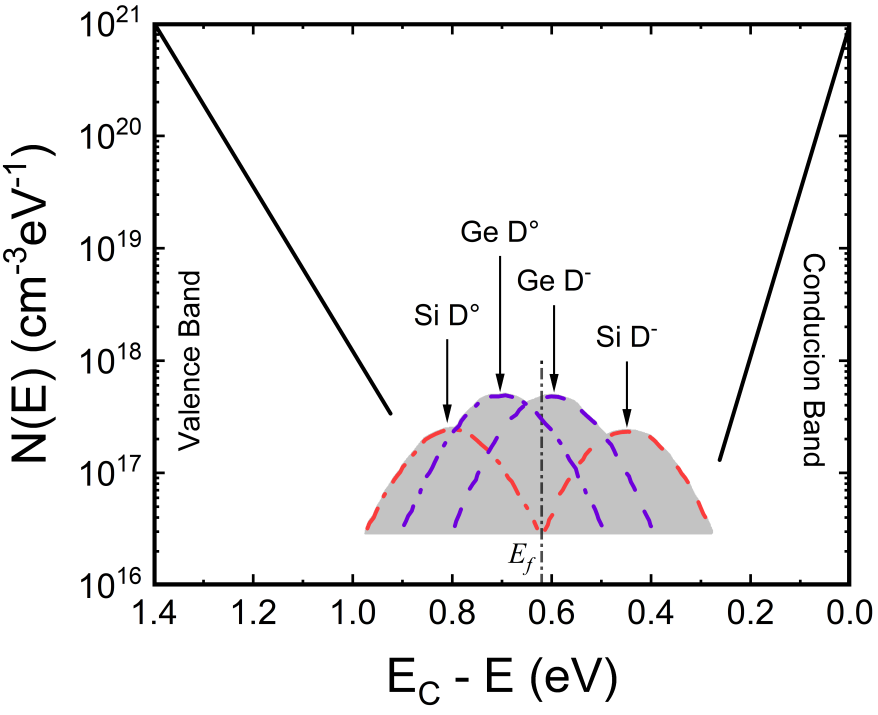

Figure 5.5: Density of states diagram of an a-$Si_{1-x}Ge_x$:H sample with Ge content $x = 0.70$. The Fermi level E_f at a particular temperature T is indicated. E_f will move as the temperature or the Ge content changes, varying therefore the Seebeck coefficient value and sign.

the second, to MPH. The cross–section of the resistor corresponding to anomalous hopping is larger than that of MPH at high temperatures, so that the current mostly flows through the anomalous hopping channel at those temperatures. As the temperature decreases, the resistances vary until the MPH channel ends up being the predominant charge transport mechanism at low temperatures. At intermediate temperatures, the resistors cross–sections, and therefore their resistances, are comparable to each other, and current flows through both channels.

The resulting thermopower for these series of samples is determined by how much current flows through each conduction channel (anomalous hopping and MPH), as

$$S = \frac{S_{AH} \times \sigma_{AH} + S_{MPH} \times \sigma_{MPH}}{\sigma_{AH} + \sigma_{MPH}}, \tag{5.4}$$

where S_{AH} and σ_{AH} are the Seebeck coefficient and dark conductivity contributions due to an anomalous hopping conduction, and S_{MPH} and σ_{MPH} are those corresponding to MPH. We can understand Eq. (5.4) as if the total thermopower S for this system were determined from the number of charge carriers in each phase (anomalous hopping or MPH) and their mobilities.

As seen in Figure 4.11 our thermopower data is limited in temperature, going from room temperature to 480 K. The conductivity analysis and the fractional conductivities in Figure 5.4, result in an MPH mechanism that is prevalent at temperatures lower than 250 K. Both these factors contribute to a very small temperature change in the 310 K $\leq T \leq$ 480 K range for the S_{MPH} parameter of each sample. We therefore assume no temperature dependence in S_{MPH}.

S_{AH} corresponds to transport between the valence band edge and states within the conduction bandtail. There is no description of the thermopower for such a transport. However, due to its similarity in nature to an activated transport mechanism, we can argue that its Seebeck coefficient will be very similar to that presented in Eq. (4.3), where E_S takes the values presented in Table 4.3 for samples with $x_{Ge} \geq 48\%$.

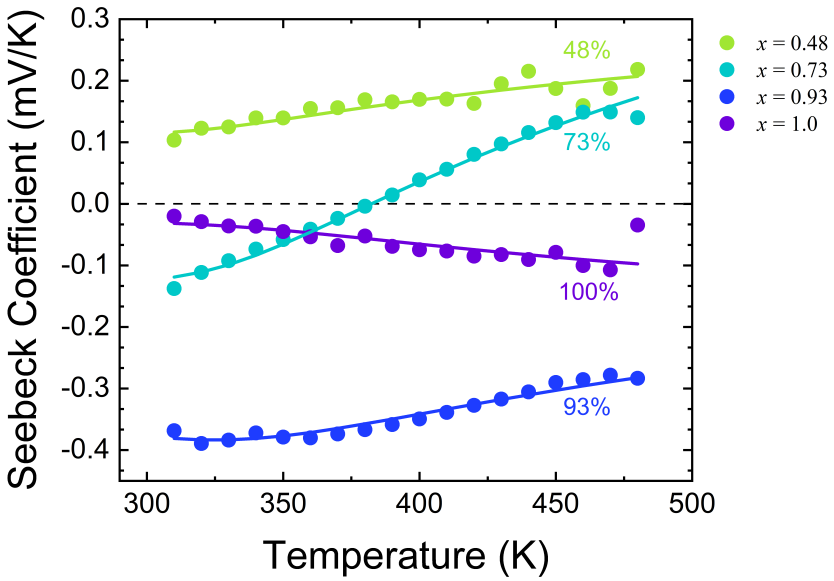

Figure 5.6: Seebeck coefficient modeling, assuming a dual–channel resistor system.

The modeling parameter S_{MPH} is expected to be in the order of the ~ 0.1 mV/K, as seen in Figure 4.11, while A should have a value close to unity, as described in Section 1.3. However, previous studies have found A values deviating from unity [51], assuming both negative and positive values, with magnitude within 10^1.

Figure 5.6 shows a plot of the calculated thermopower for the a-$Si_{1-x}Ge_x$:H samples with $x \geq 0.48$ using the dual–channel expression Eq. (5.4), which successfully describes the thermopower dependence on temperature. The parameters used to reproduce the model are listed in Table 5.2. Notice that, in order to minimize the number of fitting parameters, the E_S values (Table 4.3) were obtained from fitting the thermopower to an activated conduction, which doesn't accurately describes the data, but should give an activation energy close enough to the real one.

From these results, we can affirm that a dual–channel conduction picture is in agreement with our experimental data. The two channels are due to anomalous hopping, which is inversely dependent with temperature, more prevalent at high tem-

Sample	E_S	A	S_{MPH}
a-$Si_{52}Ge_{48}$:H	-0.09	4.6	1.3×10^{-1}
a-$Si_{27}Ge_{73}$:H	-0.31	9.7	-9.4×10^{-2}
a-$Si_{7}Ge_{93}$:H	-0.15	0.4	-3.4×10^{-1}
a-Ge:H	0.07	-2.9	-3.5×10^{-2}

Table 5.2: Resulting parameters from modeling the thermopower data of the a-$Si_{1-x}Ge_x$:H sample series with $x_{Ge} \geq 0.48$, according to Eq. (5.4). The activation energy E_S is in (eV), A is a unit–less parameter, and S_{MPH} is in (mV/K).

peratures, and an MPH mechanism, which either varies slowly with temperature or is temperature independent.

Chapter 6

Conclusions

In this thesis, I have described the synthesis and characterization of a series of a-$Si_{1-x}Ge_x$:H thin films with varying Ge content ranging from (0 – 100)%. XPS measurements are used to determine the Ge concentration. These results are qualitatively corroborated through Raman spectroscopy measurements, which show fully amorphous samples. The samples' thicknesses were determined through high–resolution profilometry measurements, showing ~ 2 μm films, with the exception of a much thinner a-Ge:H film, of 315 nm.

A commercial UV-Vis spectrometer was employed to determine the absorption spectra and bandgap of the samples series. These show a monotonic decrease in the bandgap for samples with (0 – 93)% Ge content, as expected. The a-Ge:H however, doesn't follow this trend, showing a larger bandgap than expected. This is most likely associated with being much thinner than the rest of the samples in the series, which would vary the sample's hydrogen content, and in turn, significantly change the sample's optical gap.

Measurements of the dark conductivity on these samples indicate that for Si rich samples ($x \leq 0.17$), the conductivity is well–described by an anomalous hopping expression, describing conduction through the bandtail states. Samples with higher Ge concentrations show strong evidence of a dual–channel electronic transport. At

temperatures below 250 K the dark conductivity is best described by a power–law temperature dependence. This behavior is usually ascribed to an MPH transport through the high density mid–gap defect states. Based on the resulting parameters obtained from the data analysis, it is suggested that the number of phonons needed for the hopping decreases as function of Ge content. At higher temperatures the samples show a transition between transport channels until either anomalous hopping or simple thermal activation conduction is dominant (limitations in the high temperature range make it difficult to discern between these behaviors).

Corresponding photoconductivity measurements were carried out at room temperature. These samples showed a power–law relationship as function of the power density, with exponents ranging from 0.6 to 1, and increasing with Ge content. The lowest photoconductivity values are seen for samples in the low to mid–range of Ge content. This is believed to be caused by the presence of Si and Ge dangling bonds in higher concentrations than in the a-Si:H and a-Ge:H samples.

Studies of the samples' thermopower show a transition between negative and positive Seebeck coefficients as a function of temperature and Ge content. This shift is believed to be due to a shift in the position of the Fermi level within the mid–gap states. This transition was modeled using a dual–channel picture, where the two channels' Seebeck coefficients are weighted by the MPH and anomalous hopping dark conductivities.

Measurements of the Seebeck coefficient and photoconductivity light–intensity dependence for these films are also consistent with charge transport occurring through a relatively high density of mid–gap defects, likely associated with Ge dangling bonds.

These result suggest that the concept of a mobility edge, accepted for over five decades, may in fact not be necessary to account for charge transport in certain amorphous semiconductors. However, new questions arise from the results shown in this thesis. In particular, is the power–law conductivity behavior due to multi–

phonon hopping or a different transport mechanism? How does the introduction of Ge in the matrix vary the film's DOS? Additional studies of the sensitivity of the results presented here to the deposition conditions under which the films are synthesized, as well as a wider range of amorphous semiconductors are warranted.

Chapter 7

References

[1] H. Srivastava. *Crystalline Silicon PV Market by Type (Mono–Crystalline and Multi–Crystalline) and End–User (Residential and Commercial, Utility–Scale) – Global Opportunity Analysis and Industry Forecasts, 2014–2022*. 2016.

[2] A. Reznik et al. "Avalanche multiplication phenomenon in amorphous semiconductors: Amorphous selenium versus hydrogenated amorphous silicon". In: *Journal of applied physics* 102.5 (2007), p. 053711. ISSN: 0021-8979.

[3] C.C. Wu et al. "Integration of organic LEDs and amorphous Si TFTs onto flexible and lightweight metal foil substrates". In: *IEEE Electron Device Letters* 18.12 (1997), pp. 609–612. ISSN: 0741-3106.

[4] R.A. Street. *Hydrogenated amorphous silicon*. Cambridge university press, 2005. ISBN: 0521019346.

[5] R.C. Chittick, J.H. Alexander, and H.F. Sterling. "The preparation and properties of amorphous silicon". In: *Journal of the Electrochemical Society* 116.1 (1969), p. 77. ISSN: 1945-7111.

[6] W. Schülke. "Structural investigation of hydrogenated amorphous silicon by X–ray diffraction". In: *Philosophical Magazine B* 43.3 (1981), pp. 451–468. ISSN: 1364-2812.

[7] N.F. Mott. "Electrons in disordered structures". In: *Advances in Physics* 16.61 (1967), pp. 49–144. ISSN: 0001-8732.

[8] L.K. Wagner and J.C. Grossman. "Microscopic description of light induced defects in amorphous silicon solar cells". In: *Physical review letters* 101.26 (2008), p. 265501.

[9] D.L. Staebler and C.R. Wronski. "Reversible conductivity changes in discharge–produced amorphous Si". In: *Applied physics letters* 31.4 (1977), pp. 292–294. ISSN: 0003-6951.

[10] H. Overhof and W. Beyer. "A model for the electronic transport in hydrogenated amorphous silicon". In: *Philosophical Magazine B* 43.3 (1981), pp. 433–450. ISSN: 1364-2812.

[11] J. Jang, C.H. Choi, and C. Lee. "Transport properties of hydrogenated amorphous silicon deposited by dc glow discharge decomposition". In: *Journal of Non–Crystalline Solids* 51.2 (1982), pp. 129–142. ISSN: 0022-3093.

[12] T.A. Abtew et al. "Electrical conductivity and Meyer–Neldel rule: The role of localized states in hydrogenated amorphous silicon". In: *Journal of Non–Crystalline Solids* 354.19-25 (2008), pp. 2909–2913. ISSN: 0022-3093.

[13] R. Biswas, B.C. Pan, and Y.Y. Ye. "Metastability of amorphous silicon from silicon network rebonding". In: *Physical review letters* 88.20 (2002), p. 205502.

[14] N.F. Mott. "Conduction in glasses containing transition metal ions". In: *Journal of Non–Crystalline Solids* 1.1 (1968), pp. 1–17. ISSN: 0022-3093.

[15] J. Zhang and B.I. Shklovskii. "Density of states and conductivity of a granular metal or an array of quantum dots". In: *Physical Review B* 70.11 (2004), p. 115317.

[16] L.R. Wienkes, C. Blackwell, and J. Kakalios. "Electronic transport in doped mixed–phase hydrogenated amorphous / nanocrystalline silicon thin films". In: *Applied physics letters* 100.7 (2012), p. 072105. ISSN: 0003-6951.

[17] A.L. Éfros and B.I. Shklovskii. "Coulomb gap and low temperature conductivity of disordered systems". In: *Journal of Physics C: Solid State Physics* 8.4 (1975), p. L49. ISSN: 0022-3719.

[18] K. Bodurtha and J. Kakalios. "Non–Arrhenius anomalous hopping electronic transport in hydrogenated amorphous silicon and composite amorphous / nanocrystalline thin films". In: *Journal of applied physics* 118.21 (2015), p. 215103. ISSN: 0021-8979.

[19] B.J. Western et al. "Anomalous hopping in hydrogenated amorphous silicon doped with phosphine". In: *Journal of Non–Crystalline Solids* 564 (2021), p. 120845. ISSN: 0022-3093.

[20] N. Marković et al. "Anomalous hopping exponents of ultrathin metal films". In: *Physical Review B* 62.3 (2000), p. 2195.

[21] C.J. Adkins and E.G. Astrakharchik. "Screened hopping conduction in ultrathin metal films". In: *Journal of Physics: Condensed Matter* 10.30 (1998), p. 6651. ISSN: 0953-8984.

[22] D. van der Putten et al. "Evidence for superlocalization on a fractal network in conductive carbon–black–polymer composites". In: *Physical review letters* 69.3 (1992), p. 494.

[23] A. Zabet–Khosousi et al. "Metal to insulator transition in films of molecularly linked gold nanoparticles". In: *Physical review letters* 96.15 (2006), p. 156403.

[24] A.J. Houtepen, D. Kockmann, and D. Vanmaekelbergh. "Reappraisal of variable–range hopping in quantum–dot solids". In: *Nano letters* 8.10 (2008), pp. 3516–3520. ISSN: 1530-6984.

[25] I. Shlimak et al. "Influence of parallel magnetic fields on a single-layer two-dimensional electron system with a hopping mechanism of conductivity". In: *Physical Review B* 61.11 (2000), p. 7253.

[26] K. M. Mertes et al. "Temperature dependence of the resistivity of a dilute two–dimensional electron system in high parallel magnetic field". In: *Physical Review B* 63.4 (2001), p. 041101.

[27] M. Grünewald and P. Thomas. "A hopping model for activated charge transport in amorphous silicon". In: *physica status solidi (b)* 94.1 (1979), pp. 125–133. ISSN: 0370-1972.

[28] D. Monroe. "Hopping in exponential band tails". In: *Physical review letters* 54.2 (1985), p. 146.

[29] A.G. Zabrodskii and I.S. Shlimak. "Effect of doping inhomogeneities on the conductivity of heavily doped and compensated semiconductors". In: *Soviet Physics Semiconductors* 9.3 (1975), pp. 587–589.

[30] J. Mort and D.M. Pai. *Photoconductivity and related phenomena*. distributors for the US and Canada, Elsevier/North–Holland, 1976. ISBN: 0444414630.

[31] A. Rose. *Concepts in photoconductivity and allied problems, Rev. ed.* 1978.

[32] T.D. Moustakas. "Sputtered hydrogenated amorphous silicon". In: *Journal of Electronic Materials* 8.3 (1979), pp. 391–435. ISSN: 0361-5235.

[33] M. Cutler and N.F. Mott. "Observation of Anderson localization in an electron gas". In: *Physical Review* 181.3 (1969), p. 1336.

[34] W. Beyer and J. Stuke. "Amorphous and liquid semiconductors". In: *Proceedings of the fifth international conference* (1974). Ed. by J. Stuke and W. Brenig, p. 251.

[35] W. Beyer and H. Overhof. "Transport properties of doped amorphous silicon". In: *Solid state communications* 31.1 (1979), pp. 1–4. ISSN: 0038-1098.

[36] C.H. Seager, D. Emin, and R.K. Quinn. "Electrical transport and structural properties of bulk As-Te-I, As-Te-Ge, and As-Te chalcogenide glasses". In: *Physical Review B* 8.10 (1973), p. 4746.

[37] H.J. Goldsmid and R.W. Douglas. "The use of semiconductors in thermoelectric refrigeration". In: *British Journal of Applied Physics* 5.11 (1954), p. 386. ISSN: 0508-3443.

[38] H.J. Goldsmid. *The thermal properties of solids*. Dover Publications, 1965.

[39] N.M. Johnson et al. "Stability of hydrogenated amorphous silicon deposited at high temperatures with a remote hydrogen plasma". In: *Applied physics letters* 59.12 (1991), pp. 1443–1445. ISSN: 0003-6951.

[40] W.M.M. Kessels et al. "Hydrogenated amorphous silicon deposited at very high growth rates by an expanding Ar–H_2–SiH_4 plasma". In: *Journal of applied physics* 89.4 (2001), pp. 2404–2413. ISSN: 0021-8979.

[41] A.A. Howling et al. "Frequency effects in silane plasmas for plasma enhanced chemical vapor deposition". In: *Journal of Vacuum Science & Technology A: Vacuum, Surfaces, and Films* 10.4 (1992), pp. 1080–1085. ISSN: 0734-2101.

[42] P.A. Longeway, R.D. Estes, and H.A. Weakliem. "Decomposition kinetics of a static direct current silane glow discharge". In: *The Journal of Physical Chemistry* 88.1 (1984), pp. 73–77. ISSN: 0022-3654.

[43] G. Ganguly and A. Matsuda. "Defect formation during growth of hydrogenated amorphous silicon". In: *Physical Review B* 47.7 (1993), p. 3661.

[44] D. Ritter and K. Weiser. "Suppression of interference fringes in absorption measurements on thin films". In: *Optics Communications* 57.5 (1986), pp. 336–338. ISSN: 0030-4018.

[45] G. Ghosh. "Dispersion–equation coefficients for the refractive index and birefringence of calcite and quartz crystals". In: *Optics Communications* 163.1-3 (1999), pp. 95–102. ISSN: 0030-4018.

[46] M.K Bhan, L.K. Malhotra, and S.C. Kashyap. "Electrical and optical properties of hydrogenated amorphous silicon–germanium (a-$Si_{1-x}Ge_x$:H) films prepared by reactive ion beam sputtering". In: *Journal of Applied Physics* 66.6 (1989), pp. 2528–2537. ISSN: 0021-8979.

[47] J. Tauc and A. Menth. "States in the gap". In: *Journal of Non–Crystalline Solids* 8 (1972), pp. 569–585. ISSN: 0022-3093.

[48] H.M. Dyalsingh and J. Kakalios. "Thermopower and conductivity activation energies in hydrogenated amorphous silicon". In: *Physical Review B* 54.11 (1996), p. 7630.

[49] R.A. Street et al. "The role of dangling bonds in the transport and recombination of a-SiGe:H alloys". In: *Philosophical Magazine B* 56.3 (1987), pp. 289–303. ISSN: 1364-2812.

[50] W. Paul. "Amorphous hydrogenated silicon alloys of low band–gap". In: *Proceeding of the KOSEF/NSF Joint Seminar on the Physics of Semiconductor Materials and Applications, Korea Advanced Institute of Science and Technology, Seoul, Korea* (1986), pp. 3–16.

[51] N.F. Mott and E.A. Davis. *Electronic processes in non–crystalline materials*. Oxford university press, 2012. ISBN: 0199645337.

[52] N. Robertson and L. Friedman. "IV. Non–radiative transition probabilities". In: *The Philosophical Magazine: A Journal of Theoretical Experimental and Applied Physics* 36.4 (1977), pp. 1013–1019. ISSN: 0031-8086.

[53] K. Shimakawa and K. Miyake. "Hopping transport of localized *pi* electrons in amorphous carbon films". In: *Physical Review B* 39.11 (1989), p. 7578.

[54] K. Shimakawa. "Multiphonon hopping of electrons on defect clusters in amorphous germanium". In: *Physical Review B* 39.17 (1989), p. 12933.

[55] K. Shimakawa and K. Miyake. "Multiphonon tunneling conduction of localized *pi* electrons in amorphous carbon films". In: *Physical review letters* 61.8 (1988), p. 994.

[56] K. Shimakawa. "On the mechanism of dc and ac transport in transition metal oxide glasses". In: *Philosophical Magazine B* 60.3 (1989), pp. 377–389. ISSN: 1364-2812.

[57] F. Cleri et al. "On the electrical activity of sp^2–bonded grain boundaries in nanocrystalline diamond". In: *EPL (Europhysics Letters)* 46.5 (1999), p. 671. ISSN: 0295-5075.

[58] S.C. Agarwal, S. Guha, and K.L. Narasimhan. "AC conductivity in amorphous germanium". In: *Journal of Non-Crystalline Solids* 18.3 (1975), pp. 429–437. ISSN: 0022-3093.

[59] N. Aoki, K. Nara, and Y. Ochiai. "Coulomb gap energy in amorphous Si_xGe_{1-x} films". In: *Physica Status Solidi (b)* 218.1 (2000), pp. 5–9. ISSN: 0370-1972.

[60] A. Morimoto et al. "ESR and IR Studies on a-$Si_{1-x}Ge_x$:H prepared by glow discharge decomposition". In: *Japanese journal of applied physics* 20.11 (1981), p. L833. ISSN: 1347-4065.

[61] M. Kumeda et al. "NMR and ESR studies on a-$Si_{1-x}Ge_x$:H prepared by magnetron sputtering". In: *Solid state communications* 55.5 (1985), pp. 409–412. ISSN: 0038-1098.

[62] W. Paul, R.A. Street, and S. Wagner. "Hydrogenated amorphous semiconductors". In: *Journal of Electronic Materials* 22.1 (1993), pp. 39–48. ISSN: 0361-5235.

[63] M. Stutzmann and J. Stuke. "Paramagnetic states in doped amorphous silicon and germanium". In: *Solid state communications* 47.8 (1983), pp. 635–639. ISSN: 0038-1098.

[64] N. Robertson and L. Friedman. "Non–radiative transitions". In: *The Philosophical Magazine: A Journal of Theoretical Experimental and Applied Physics* 33.5 (1976), pp. 753–774. ISSN: 0031-8086.

[65] R. Atta–Fynn, P. Biswas, and D.A. Drabold. "Electron–phonon coupling is large for localized states". In: *Physical Review B* 69.24 (2004), p. 245204.

[66] K. Prasai, P. Biswas, and D.A. Drabold. "Electrons and phonons in amorphous semiconductors". In: *Semiconductor Science and Technology* 31.7 (2016), p. 073002. ISSN: 0268-1242.

[67] I.P. Zvyagin. "The hopping thermopower". In: *Hopping Transport in Solids* 28 (1991), pp. 143–174.